TEMPLATE ULTRAVIOLET TO NEAR-INFRARED SPECTRA OF STAR-FORMING GALAXIES AND THEIR APPLICATION TO K-CORRECTIONS

Anne L. Kinney,[1,3,4,5] Daniela Calzetti,[1,3,4] Ralph C. Bohlin,[1,4] Kerry McQuade,[1]
Thaisa Storchi-Bergmann,[2,5] and Henrique R. Schmitt[1,2,6]

ABSTRACT

Template UV-optical spectra of quiescent and starburst galaxies are presented and used to derive K-corrections as a function of morphological type and redshift. IUE observations and archival data are used for the UV template spectra. The optical spectra are from ground-based observations obtained in apertures that match closely the 200 arcsec^2 IUE aperture. The templates of quiescent galaxies are built according to morphological type, elliptical, bulge, S0, Sa, Sb, and Sc, and the templates of starburst galaxies according to color excess. The unprecedented characteristics of these templates is that UV and optical spectra have been obtained in matched apertures to produce consistent spectral information from 1200 to 10,000 Å. Despite the relatively small IUE aperture, the galaxy stellar populations are well represented in the elliptical, S0, Sa, and Sc, and in the starburst templates. The spectra are available digitally.

The UV-optical templates can be applied to the classification of high-redshift galaxies and to the identification of the host galaxies of quasars.

The templates predict that observed magnitudes from traditional ground-based photometric surveys can be uniquely interpreted. For example, U, B, and I magnitudes uniquely determine both the redshift and the morphological type of a galaxy. The template spectra are also used to calculate K-corrections for galaxies as a function of morphological type and redshift, up to z = 2. These improved K-corrections are not sufficient to explain the excess counts in faint blue galaxies.

A subset of our galaxy templates are linked with published data from the radio to the X-ray for galaxies and quasars. A comparison between the quiescent galaxies and the quasars suggests that, in the optical band, the host galaxy is a factor of 10–100 fainter in flux than the quasar.

Subject headings: galaxies: distances and redshifts — galaxies: photometry — galaxies: starburst — galaxies: stellar content — quasars: general

1. INTRODUCTION

As searches for faint, primeval galaxies continue, the number of unresolved questions grows. Faint galaxy counts reveal more blue galaxies than predicted based on local galaxy counts; however, the predicted number of red galaxies is about right. The number counts raise the question of the relation between local galaxies and early galaxies: did the numerous early galaxies merge to create present-day galaxies as suggested by Broadhurst, Ellis, & Glazebrook (1992), or did an initial burst of star formation make small galaxies temporarily bright? When did the first galaxies form, and what is the best method to find these primeval galaxies? More specifically, how does the first epoch of star formation compare with later epochs, where the stars are made of processed gas?

Here, we produce spectral energy distributions (SEDs) for local galaxies from the ultraviolet to the near-infrared, in order to *relate morphological type to spectral energy dis-*

tribution. Observations in the ultraviolet allow corrections to colors (K-corrections) to be calculated as a function of redshift up to z ~ 2 for each morphological class.

A large aperture spectrum of a galaxy contains elements from physically different regions of the galaxy and is more complex than the spectrum of a single star. Dust extinction complicates the interpretation of the spectrum, since a dusty galaxy is expected to be relatively opaque in the UV and relatively transparent in the IR.

The contributors to a galaxy's UV, optical, and near-IR spectrum are hot stars, cool stars, H II regions, and the interstellar medium (ISM). The wavelength region shortward of 912 Å is dominated by O star emission and interstellar absorption by H I. Early-type OB stars are responsible for the UV continuum and absorption lines longward of 1200 Å. Cool stars contribute the longer wavelength continuum and most of the long wavelength absorption lines. The UV to IR spectrum samples a wide range in population from young (less than 10^7 yr) to old stars. H II regions are evidenced by the presence of emission lines, and the ISM creates certain absorption lines (e.g., Tables 4–7 in Kinney et al. 1993).

We present template spectra of elliptical, bulge, S0, Sa, Sb, Sc, and starburst galaxies in a matched 10″ × 20″ aperture from 1200 Å to 8000 Å, and in some cases to 10,000 Å. The observations are presented in § 2, and the procedure adopted to produce the templates in § 3. The general properties of the templates are discussed in § 4.1. Applications of the templates to the classification of high-redshift galaxies and to the identification of the host galaxies of

[1] Space Telescope Science Institute, 3700 San Martin Drive, Baltimore, MD 21218.

[2] Instituto de Física, Universidade Federal Rio Grande do Sul C.P. 15051, Porto Alegre, RS, 91501-970, Brazil.

[3] Visiting Astronomers, Kitt Peak National Observatory, National Optical Astronomy Observatories, which is operated by AURA, Inc., under a cooperative agreement with the National Science Foundation.

[4] Guest Investigators with the IUE Observatory.

[5] Visiting Astronomers, Cerro Tololo Inter-American Observatory (CTIO), National Optical Astronomy Observatories, which is operated by AURA, Inc., under a cooperative agreement with the National Science Foundation.

[6] CNPq fellow.

TABLE 1

ATLAS GALAXIES

Site	IUE	Galaxy Name	Morphological Type	Radius	v_H (km s^{-1})	B_T	M_B ($H_0 = 50$)	$E(B-V)_{MW}$	Other Names
CTIO	S + L	NGC 210	Sb	2′30″	1768	11.65	−21.86	0.01	
KPNO	S + L	NGC 224	Sb	80 00	−297	4.38	−21.61	0.08	M31
KPNO	S + L	NGC 598	Scd	35 24	−180	6.26	−19.07	0.04	M33
KPNO	L	NGC 1023	SB0	4 33	661	10.36	−21.17	0.06	
...	S + L	NGC 1058	Sc	1 30	518	12.15	−19.27	0.06	
CTIO	S + L	NGC 1399	E1 pec	3 27	1465	10.79	−21.61	0.00	
CTIO	S + L	NGC 1404	E2	1 39	1994	11.06	−21.34	0.00	
CTIO	S + L	NGC 1433	SBab	3 15	1061	10.68	−21.15	0.00	
CTIO	S + L	NGC 1553	S0 pec	2 15	1236	10.42	−21.26	0.00	
...	S + L	NGC 1637	Sc	2 00	717	11.82	−19.72	0.03	
KPNO	S + L	NGC 2403	Sc	10 57	131	8.89	−19.47	0.04	
...	S + L	NGC 2681	Sa	1 48	715	11.09	−20.48	0.02	
...	S + L	NGC 2841	Sb	4 03	637	10.17	−21.53	0.00	
KPNO	S + L	NGC 3031	Sb	13 27	−36	7.86	−20.75	0.04	M81
...	S	NGC 3432	Sc	3 24	616	11.73	−19.50	0.00	
...	S + L	NGC 3994	Sc	30	3096	13.30	−20.81	0.01	
...	L	NGC 4102	Sb	1 30	865	12.30	−19.80	0.00	
...	S + L	NGC 4259	Sc	36	2487	14.55	...	0.00	
...	S + L	NGC 4314	SBa pec	2 06	883	11.35	−19.80	0.02	
...	L	NGC 4350	S0	1 30	1184	11.88	−19.82	0.01	
...	S + L	NGC 4382	S0 pec	3 33	739	10.10	−21.60	0.01	M85
CTIO	L	NGC 4569	SABab	4 45	−261	10.23	−22.31	0.02	M90
CTIO	S + L	NGC 4594	Sa	4 21	1089	9.28	−22.81	0.03	M104
...	S + L	NGC 4736	SAab	5 36	311	8.92	−20.81	0.00	M94
...	S + L	NGC 4826	Sb	5 00	413	9.37	−20.61	0.04	M64
...	S + L	NGC 5194	Sbc	5 36	464	8.98	−21.60	0.00	M51a
KPNO	S + L	NGC 6340	SA(s)0/a	1 42	1234	11.90	−21.05	0.05	
CTIO	S	NGC 6868	E2	1 45	2764	11.83	−21.93	0.04	
CTIO	S + L	NGC 7083	Sb	1 57	3089	11.80	−22.81	0.02	
CTIO	S + L	NGC 7196	E3	1 15	2981	12.46	−21.37	0.00	

NOTES.—The first column lists the observatory where the optical spectra for each galaxy were obtained (KPNO or CTIO). The second column specifies if the UV spectra consisted of data from both the *IUE* Short-Wavelength and Long-Wavelength Cameras (S + L) or from one of the two (S or L). The morphological type follows, where possible, the classical Hubble classification. The radius is half the largest diameter for the galaxy as given in NED. The heliocentric velocity (v_H) and the apparent magnitude (B_T) are from the Revised Shapley-Ames Catalogue (RSA), for from The Third Reference Catalogue of Bright Galaxies (RC3). M_B is the absolute magnitude calculated from the apparent magnitude corrected for Galactic absorption and from the recession velocity reduced to the centroid of the Local Group (cf. RSA). The reddening $E(B-V)_{MW}$ from our Galaxy is from Burstein & Heiles 1984.

quasars are shown in §§ 4.2 and 4.3, respectively. Color-color diagrams and *K*-corrections are produced in § 4.4. Finally, we compare our observed SEDs with those produced by stellar population models in § 4.5.

The template spectral energy distributions and their 1 σ standard deviations are presented in the Appendix, along with averages and standard deviations in 200 Å bins. Diagrams of color versus redshift and color versus color for the morphological types are also presented in the Appendix.

2. OBSERVATIONS AND DATA ANALYSIS

The template SEDs are derived from the UV and optical spectra of the central regions of 30 quiescent galaxies, which cover morphological types from elliptical to Sc, and of the central regions of 39 starburst galaxies, which are mainly irregular and galaxies with disturbed morphologies (Calzetti, Kinney, & Storchi-Bergmann 1994; McQuade, Calzetti, & Kinney 1995; Storchi-Bergmann, Kinney, & Challis 1995).

The UV spectra for six of the quiescent galaxies were taken with the *IUE* during observing campaigns in 1992 and 1993 as part of a program to produce templates of normal galaxies. The remaining UV spectra are archival *IUE* spectra collected in the atlas of Kinney et al. (1993) and the atlas of Koratkar et al. (1996). The UV spectra cover the

wavelength range 1200–3200 Å with a resolution of about 6 Å. The UV spectra used in the templates are corrected for Galactic extinction based on the $E(B-V)$ values listed in Table 1 of Kinney et al. (1993) and using the UV extinction curve of Seaton (1979). In all but one spectrum, NGC 1569, this effect is very small. Approximately half the optical spectra were obtained at the CTIO 1 m telescope with the two-dimensional Frutti detector for the visible range and at the 1.5 m telescope with a CCD detector for the near-IR wavelength range (Storchi-Bergmann et al. 1995). A long slit with a 10″ width was used, and a window 20″ long was extracted to match the 200 arcsec^2 *IUE* aperture. The CTIO spectra cover the wavelength range 3200–10,000 Å with a resolution ~8 Å. The remaining optical spectra were obtained at the KPNO 0.9 m with the intensified Reticon spectrograph, using a circular aperture of 13″.5 diameter. The KPNO spectra cover the wavelength range 3200–7700 Å with a resolution of 10 Å (McQuade et al. 1995). The difference in flux attributable to the difference in size between the optical and the *IUE* apertures is the difference in size convolved with the flux distribution within the aperture and is therefore less than 30%, which is within the uncertainty of the absolute calibration of the optical fluxes, so that no normalization has been done. Details on the reduction and calibration of the spectra can be found in

Kinney et al. (1993), McQuade et al. (1995), and Storchi-Bergmann et al. (1995).

Table 1 lists the 30 quiescent galaxies used in the elliptical and spiral templates, along with the galaxy name, the morphological type, the size, the redshift, the apparent and absolute blue magnitudes ($H_0 = 50$ km s^{-1} Mpc^{-1}), and the foreground reddening from the Milky Way [$E(B-V)_{MW}$; see Burstein & Heiles 1984]. Comparable information on the 39 starburst galaxies can be found in Calzetti et al. (1994).

3. THE TEMPLATES

3.1. *How the Templates Are Built*

The quiescent galaxies are grouped according to morphological type: E (elliptical), S0, Sa, Sb, and Sc, respectively, as shown in Table 2. The UV and optical spectra of the Sb galaxies NGC 224 (M31) and NGC 3031 (M81) are dominated by the stellar population in the bulge, and therefore the two galaxies form a separate group, the bulge template. The starburst galaxies are grouped in six classes

TABLE 2

GALAXIES INCLUDED
IN TEMPLATES

UV	Optical
Elliptical	
NGC 1399	NGC 1399
NGC 1404	NGC 1404
NGC 6868	NGC 6868
NGC 7196	NGC 7196
Bulge	
NGC 224	NGC 224
NGC 3031	NGC 3031
S0	
NGC 1023	NGC 1023
NGC 1553	NGC 1553
NGC 4350	...
NGC 4382	...
NGC 6340	NGC 6340
Sa	
NGC 1433	NGC 1433
NGC 2681	...
NGC 4314	...
NGC 4594	NGC 4594
NGC 4569	NGC 4569
NGC 4736	...
Sb	
NGC 210	NGC 210
NGC 2841	...
NGC 4102	...
NGC 4826	...
NGC 7083	NGC 7083
Sc	
...	NGC 598
NGC 1058	...
NGC 1637	...
NGC 2403	NGC 2403
NGC 3432	...
NGC 3994	...
NGC 4259	...
NGC 5194	...

according to increasing values of the intrinsic color excess $E(B-V)$, as derived from the ratio of the Balmer emission lines Hα/Hβ: from $E(B-V) \simeq 0.05$ to $E(B-V) \simeq 0.65$ (see Table 3 in Calzetti et al. 1994). Calzetti et al. (1994) established that dust obscuration, i.e., the intrinsic color excess, is the dominant parameter that determines the appearance of the starburst SED.

The template for the elliptical galaxies includes only those galaxies that have a narrow range of Mg2 indexes and comparable absolute magnitudes to avoid the well-known color-luminosity relation of ellipticals. The Mg2 indexes of the included galaxies are NGC 1399 = 0.334, NGC 1404 = 0.317, NGC 6868 = 0.317, and NGC 7196 = 0.286 (Burstein et al. 1988). In Table A1, it can be seen that the elliptical template has a low signal-to noise ratio (S/N). The 1σ standard deviation quoted in Table A1 is dominated by the uncertainty in the spectra rather than in the intrinsic differences between the galaxies. To demonstrate this, note that the average fluxes, standard deviations, and signal-to-noise ratios for the individual galaxies in the spectral regions 1500–1900 are NGC 1399, $F_\lambda = 0.070 \pm 0.014$, S/N = 5.1; NGC 1404, $F_\lambda = 0.035 \pm 0.039$, S/N = 0.9; NGC 6868, $F_\lambda = 0.052 \pm 0.076$, S/N = 0.7; and NGC 7196, $F_\lambda = 0.112 \pm 0.109$, S/N = 1.0. The details of the individual spectra will be presented in Koratkar et al. (1996).

To what degree are the templates affected by aperture effects? The differences in SEDs of individual galaxies do not show evidence of being correlated to the size or distance of the galaxy, as would be expected if the galaxies' spectra were dominated by aperture effects. For example, the galaxies making up the Sa template, NGC 1433, NGC 2681, NGC 4314, NGC 4594, and NGC 4736, have a factor of over 2 in galaxy size, with the galaxies having radii of 3'15", 1'48", 2'06", 4'21", and 5'36", respectively, but only a small range of distance to the galaxy (18.5, 16, 17, 17.5, and 6.9 Mpc, respectively). Meanwhile, their UV slopes (with values -0.95 ± 0.28, 0.17 ± 0.40, -0.07 ± 0.35, -1.23 ± 0.44, and 0.27 ± 0.17, respectively), which serve as a rough measure of their overall SED, do not track with galaxy radius or show a trend for distant galaxies to be bluer than nearby galaxies, or a trend for small galaxies to be bluer than large galaxies, as would be the case if the individual SEDs were dominated by aperture effects. For example, NGC 1433 and NGC 4314 have similar radii (3'15" and 2'06", respectively) and similar distances (18.5 and 17.0 Mpc, respectively), but have very different UV slopes (-0.95 ± 0.28 and 0.07 ± 0.35). The differences between galaxies thus appear to be due to intrinsic differences rather than to aperture effects.

In order to make the templates, all the spectra are shifted to the rest frame and corrected for the foreground Galactic extinction using the Seaton (1979) extinction curve. Within each starburst group, the UV-optical spectra are rescaled to a common flux value and are averaged, after weighting each spectrum by its signal-to-noise ratio, to produce the final template. The templates of the quiescent galaxies are constructed by averaging separately the UV and optical spectra, since not all the quiescent galaxies observed at UV wavelengths were observed in the optical as well (Table 2). Within each morphological group, the optical spectra are averaged after rescaling the fluxes to a common value and weighting each spectrum by the exposure time. This is analogous to the S/N weighting procedure, since the optical spectra of the quiescent galaxies do not show a large range
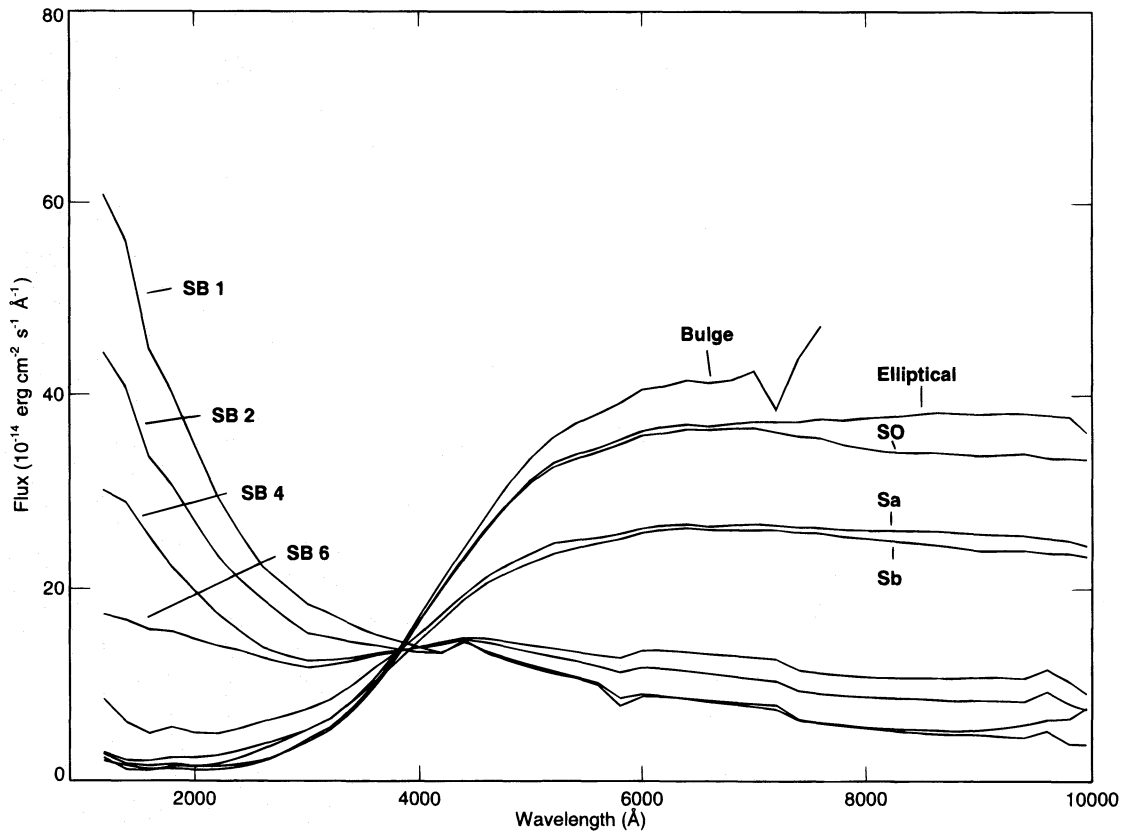
FIG. 1.—The spectra binned in 200 Å bins are shown between 1200 and 10,000 Å, normalized at 4000 Å for the bulge, elliptical, S0, Sa, Sb, and starburst galaxies with varying dust content. The starburst galaxy templates are grouped according to the mean color excess value $E(B-V)$ and are labeled as SB1 for $E(B-V) < 0.10$; SB2 for $0.11 \leq E(B-V) \leq 0.21$; SB4 for $0.39 \leq E(B-V) \leq 0.50$; and SB6 for $0.61 \leq E(B-V) \leq 0.70$.

in flux level. The UV spectra are averaged according the same procedure adopted for the starburst spectra.

The templates are presented in Figure 1, normalized to the flux at 4000 Å. This normalization is chosen to empha-size the spectral difference between the morphological types. The individual templates and their 1 σ standard devi-ations are shown in Figures 2a–2l. Because the spectra have been taken in large apertures, the strong night skyline around 5500 Å is difficult to remove and has been masked in most of the plots.

3.2. Digital Distribution of the Template

The templates, and the multiwavelength spectra of the individual galaxies on which they were based, will be avail-able in digital form through the National Space Science Data Center (NSSDC), via ftp at host ftp.stsci.edu, and eventually through the Data Archive and Distribution System (DADS) at STScI. The files will be available both in FITS format and in ASCII. Electronic mail requests for the NSSDC can be directed to archives@ndadsa.gsfc.nasa.gov, or via nssdc.gsfc.nasa.gov. The host ftp.stsci.edu (130.167.1.2) will contain the data in the directory catalogs/spectra.

4. TEMPLATE APPLICATIONS

4.1. General Properties

The early-type galaxies (E, bulge, and S0) have the reddest spectra, with the largest increase in flux from the UV to the optical (see Fig. 1). The Sa and Sb galaxies have a slightly weaker increase, while the spectra of the Sc galaxies

tend to be rather flat. The sequence of spectral shapes from E to Sc mirrors the increasing contribution of the disk stellar population relative to the bulge population going from early to late Hubble types. Starburst galaxies become increasingly bluer, with a spectrum that rises toward shorter wavelengths, as the dust obscuration, i.e., $E(B-V)$, decreases.

The E, bulge, S0, Sa, and Sb galaxies have very similar spectral shapes and absorption features for $\lambda > 5000$ Å, and would be rather indistinguishable from their broadband optical and near-IR colors (cf. Kennicutt 1992). The E and S0 templates have similar UV spectra and 4000 Å Balmer discontinuities. The strength of the 4000 Å discontinuity decreases from the E and S0 templates to the Sa and the Sb templates.

Our templates are made of galaxies with a variety of physical properties (cf. Table 1), which is important for building representative "galaxy spectral templates." However, the galaxies also show a variety of sizes, and the *IUE* aperture, although it is the largest available for UV spectroscopy, samples only their inner 15″ region. The aperture/galaxy size mismatch is not a problem for the star-burst templates, because their integrated spectral character-istics are dominated by the central burst of star formation (cf. Calzetti et al. 1995). The mismatch is not likely to be a problem for the early Hubble types (E, bulge, and S0), because their integrated emission is dominated by the bulge stellar population, and the inner regions can be considered representative of the galaxies as a whole.

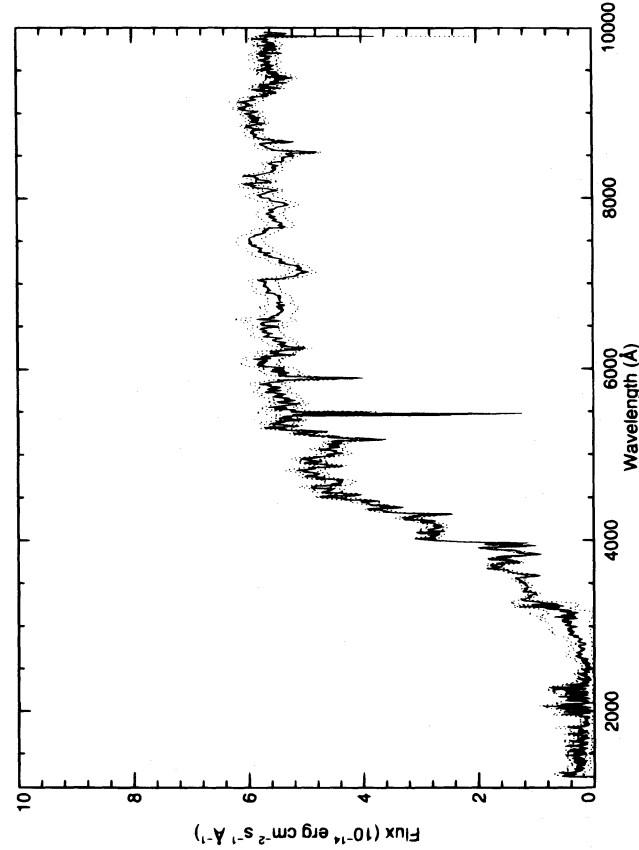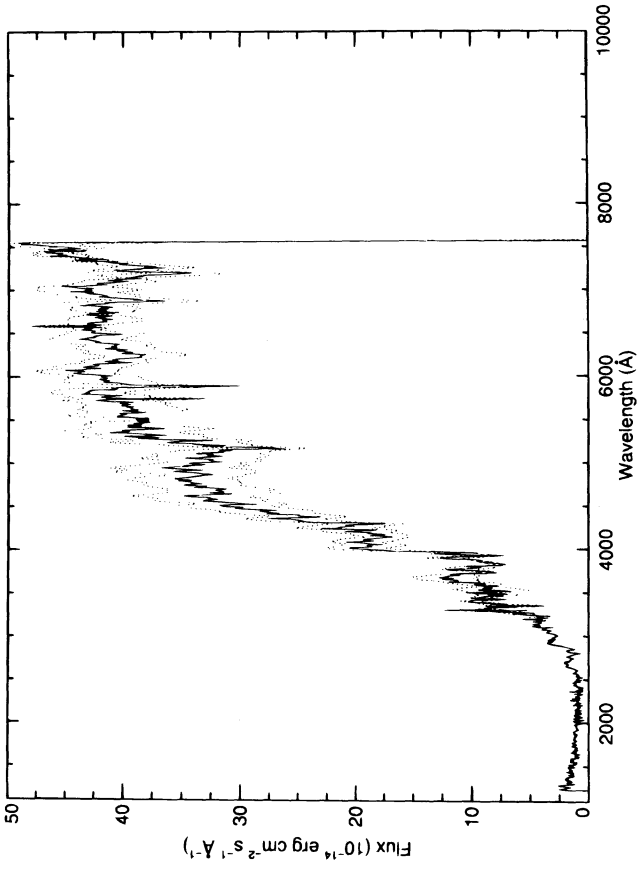A direct comparison of our templates with Kennicutt's

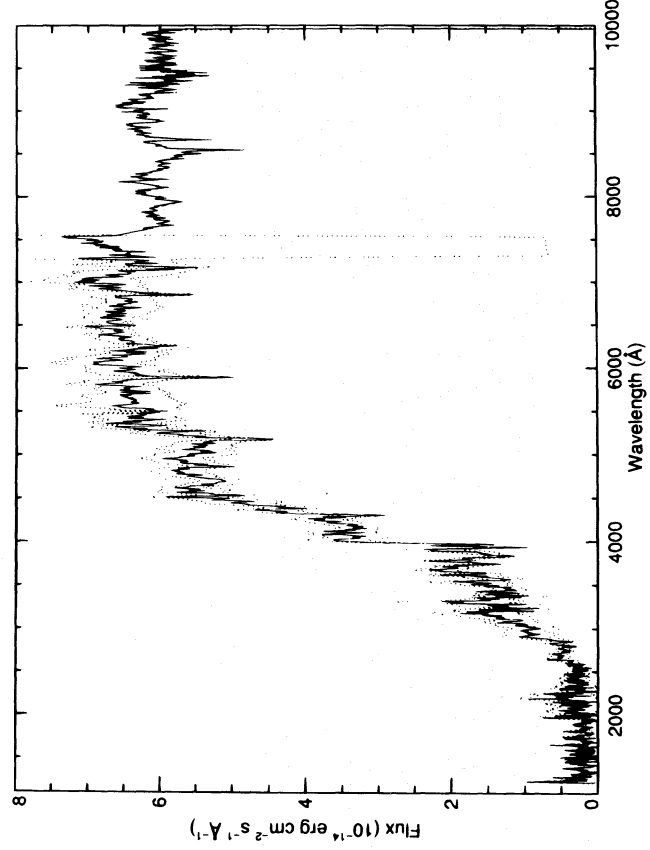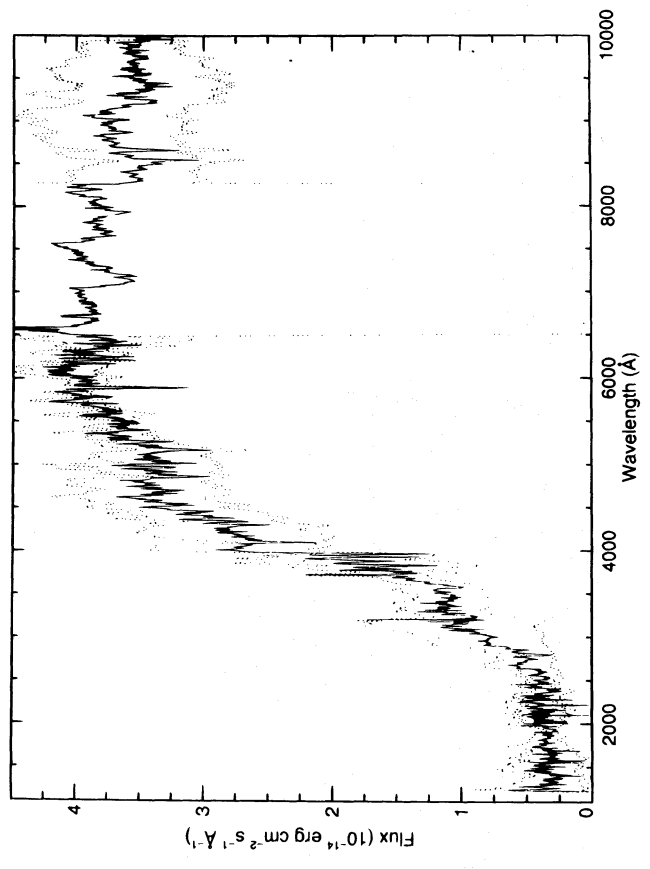FIG. 2.—The individual templates, together with the 1 σ standard deviation of the spectra combined to form the template. The weighted average of the flux is given by the solid line. The weighted standard deviation of the normalized spectra co-added to form the template is given by the dotted line. (a) Elliptical, (b) bulge, (c) S0, (d) Sa, (e) Sb, (f) Sc, (g) starburst with $E(B - V) < 0.10$, (h) starburst with $0.11 \leq E(B - V) \leq 0.21$, (i) starburst with $0.25 \leq E(B - V) \leq 0.35$, (j) starburst with $0.39 \leq E(B - V) \leq 0.50$, (k) starburst with $0.51 \leq E(B - V) \leq 0.60$, and (l) starburst with $0.61 \leq E(B - V) \leq 0.70$.
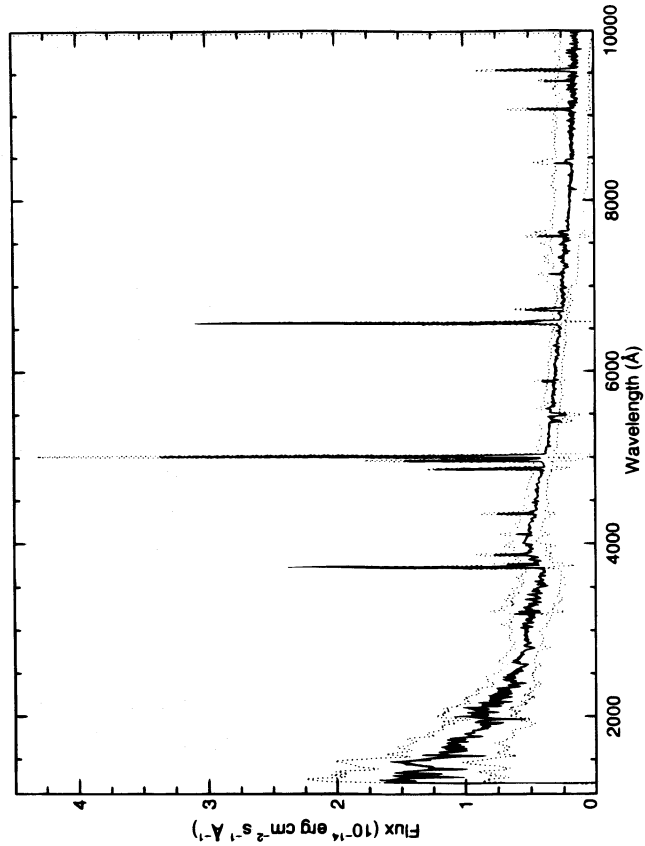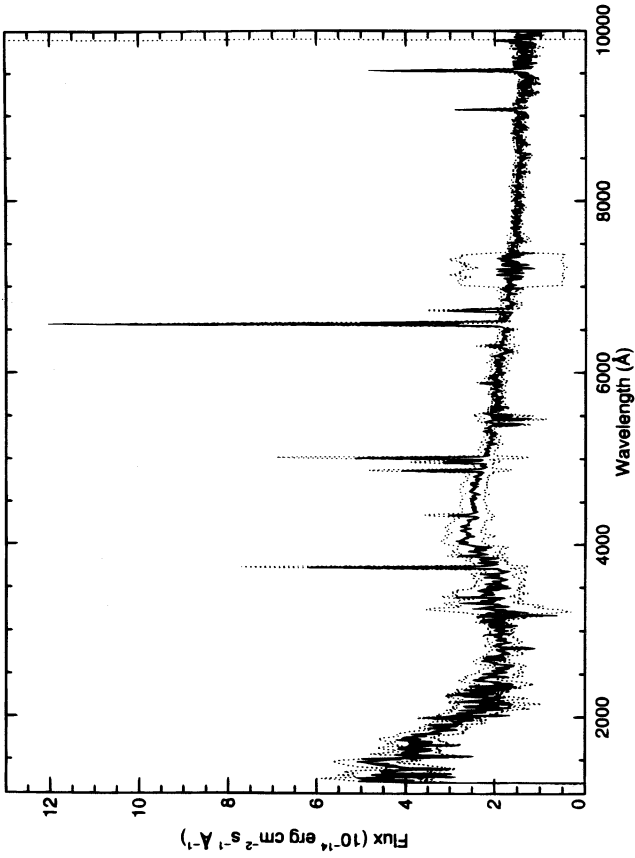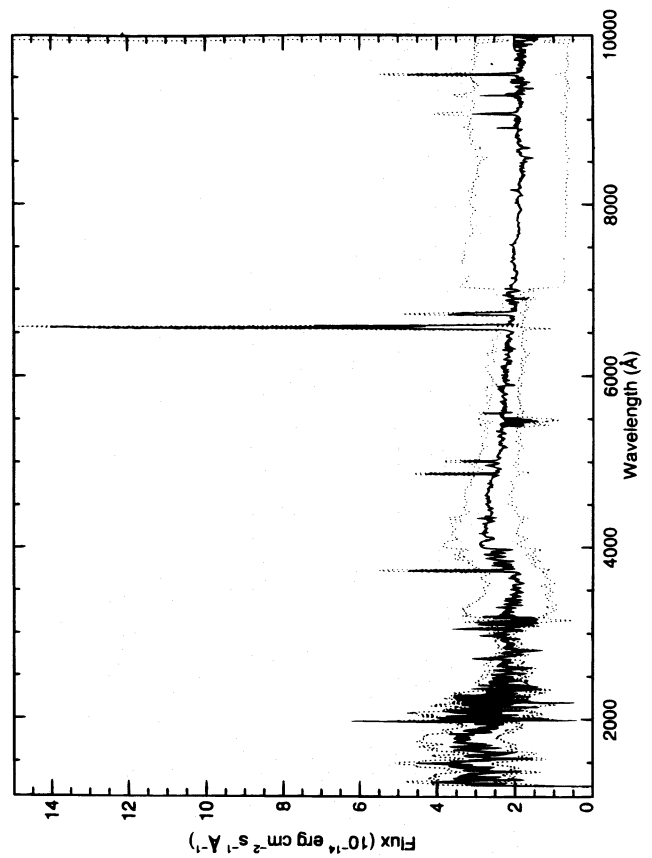
42
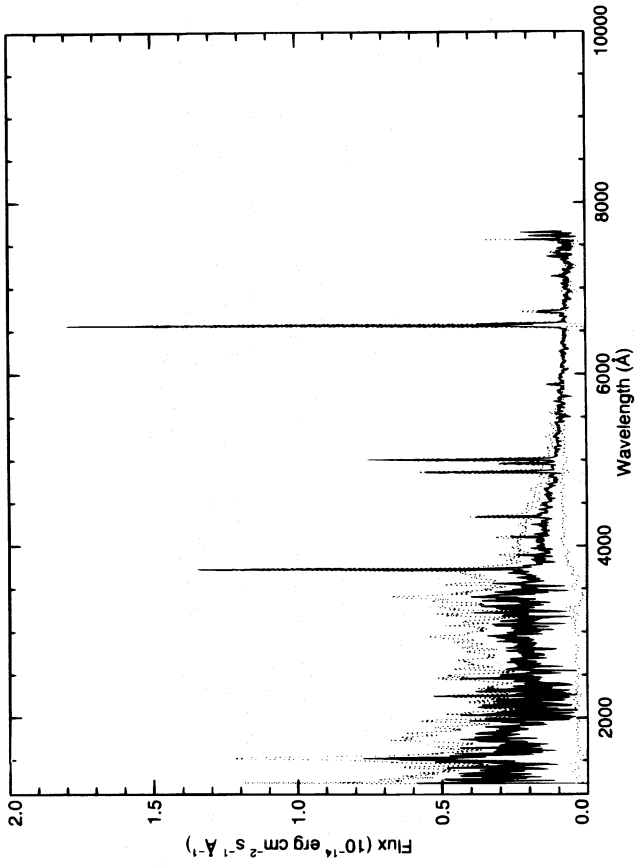
Fig. 2e

Fig. 2f
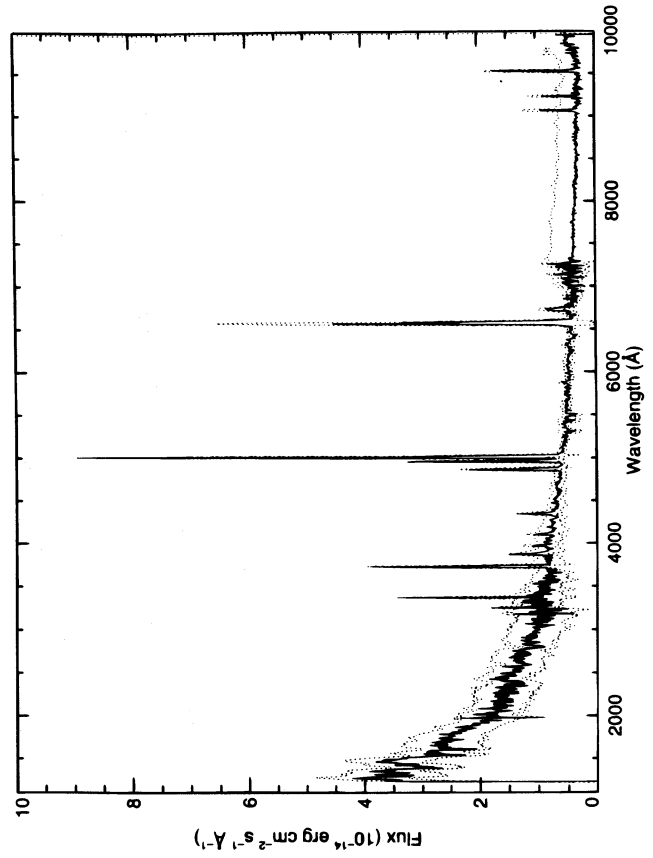
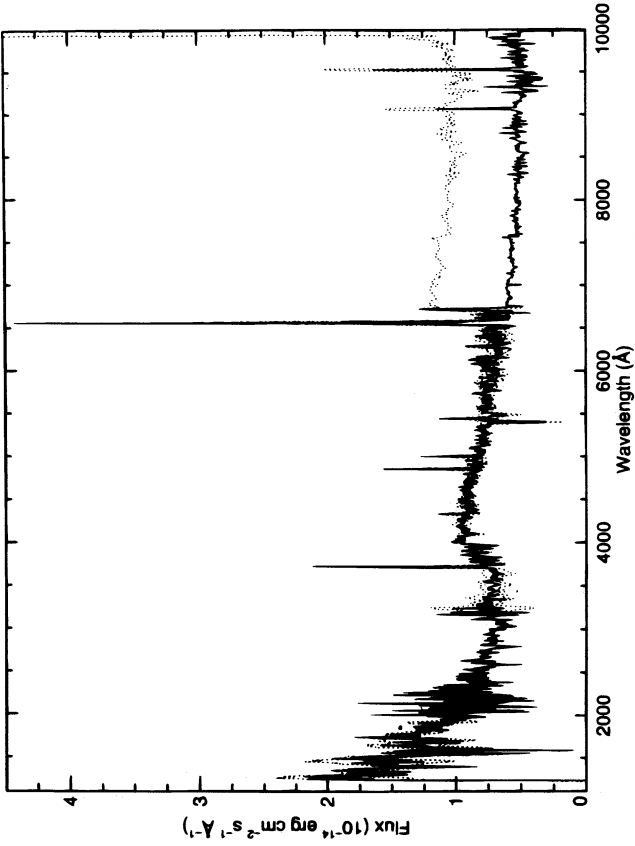Fig. 2g

Fig. 2h
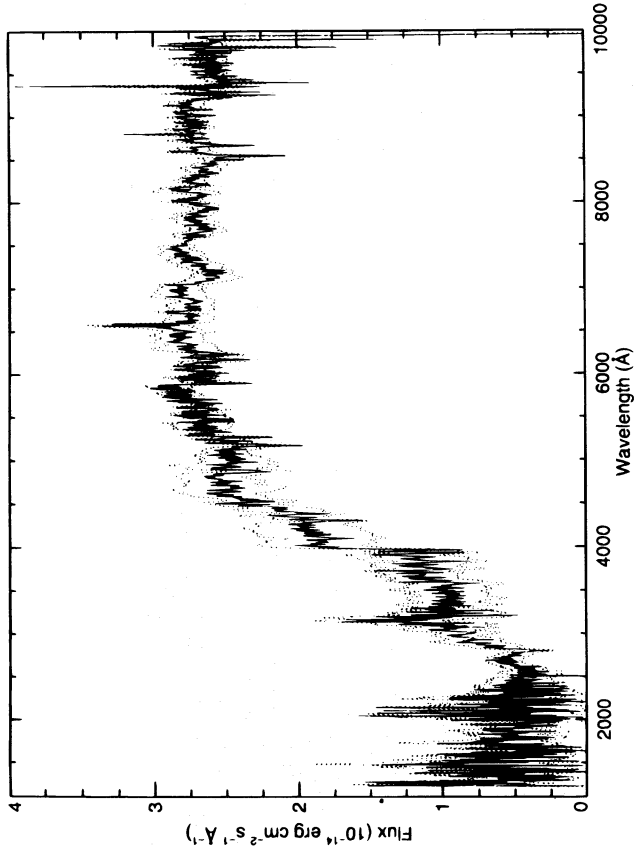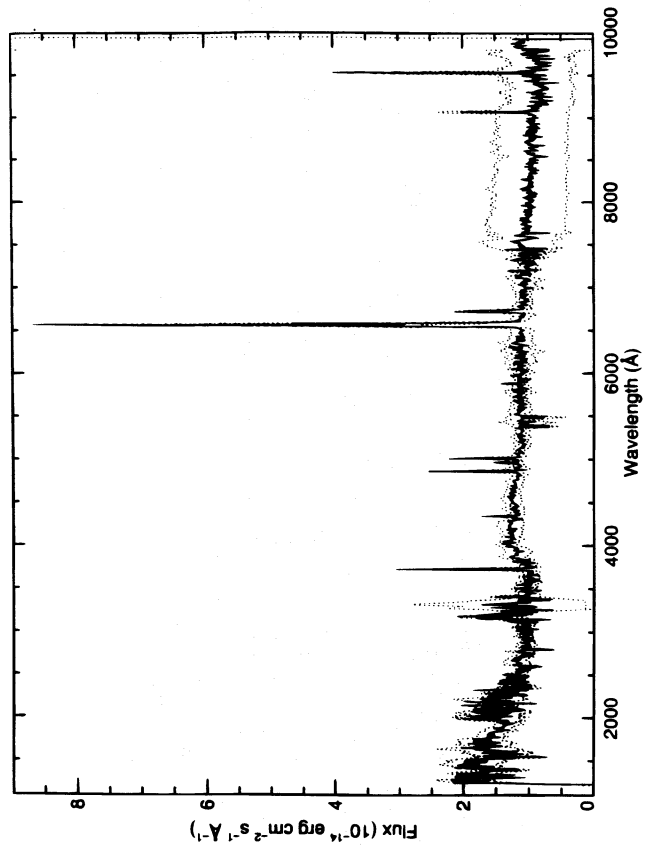
Fig. 2i

Fig. 2j

Fig. 2k

Fig. 2l

(1992) large aperture ($\sim 90''$) optical spectra of quiescent galaxies shows that our E, S0, Sa, and Sc templates are representative of the galaxies global properties. However, our Sb template underestimates the younger disk stellar population relative to the old bulge population. This conclusion is based mostly on the comparison between the emission-line strengths: our Sb template shows weaker nebular emission lines than Kennicutt's Sb spectra, meaning that the template underrepresents the youngest stellar populations, which dominate in the external galaxy regions.

The main selection criterion for the galaxies in the sample is their detectability at UV wavelengths, and therefore the sample of quiescent galaxies, which have weak UV fluxes, includes only bright, local galaxies, while the sample of starburst galaxies, which have a large range in UV brightness, includes galaxies up to redshift $z \sim 0.03$. Therefore, the templates of quiescent galaxies give the spectral shapes as a function of galaxy type but give little information on spectral shape as a function of luminosity (cf. next section).

4.2. *Identification of High-Redshift Galaxies*

The identification of high-redshift galaxies is hampered by the general lack of emission lines in the galaxy spectra for deriving secure redshifts. The quiescent galaxies are distinguished mainly by the difference in their UV and optical continuum shape. Only the starburst galaxies show emission lines, and those emission lines appear only in the optical region. The shortest wavelength emission line in starburst galaxies is [O III] $\lambda 3727$, which is already shifted into the I band at a redshift of a little more than 1.0.

Can colors be used to identify galaxies and derive their redshift? Not easily. If the redshift is known, for example, in the case of a galaxy discovered through narrowband imaging in the redshifted light of Lyα (for a review see Giavalisco, Macchetto, & Sparks 1994), the observed color will distinguish between morphological types, as can be seen in Figures 3a and 3b. However, if both the redshift and the morphological type must be determined simultaneously, the problem is more difficult. The slopes of the optical continuum longward of 5000 Å and the slopes of the UV continuum shortward of 3000 Å do not vary substantially between the different morphological types. Thus, the predominant identifying and differentiating feature in the SEDs of the different types of galaxies is their behavior between 3000 and 5000 Å, i.e., the 4000 Å Balmer discontinuity. The 4000 Å discontinuity is the strongest for the bulge and E galaxies and grows progressively weaker for the S0, Sa, and Sb galaxies. In the starburst galaxies, the spectra will show a reversal at 4000 Å; at shorter wavelengths, they increase in flux inversely proportional to their dust content (see Calzetti et al. 1994).

A better approach may be to use observed magnitudes directly, in order to derive a robust description of morphological type and redshift of galaxies, as described in detail in Connolly et al. (1995). The templates for the E, Sa, Sb, and Sc galaxies are shown in Figure 4, redshifted through the U, B, and I bandpasses to produce a grid of magnitudes for each template as a function of redshift. The galaxies form a well-defined plane in the U, B, I cube. Given multiple bandpasses of information on a large survey of galaxies, such as will be produced in the Sloan Survey (Gunn & Knapp 1992), statistical identifications can be made based on a comparison between the data and the templates.

Characterizing the thickness of the plane within the U, B, I cube would be useful. In other words, how do the colors depend on luminosity for each morphological type? As discussed above, the galaxies making up the sample have little range in luminosity since the *IUE* satellite can detect only the brightest, nearby galaxies, so this data set cannot address the spectral dependencies on luminosity.

4.3. *Identifying the Host Galaxies of Quasars*

Our spectral energy distributions can be joined with published data in other wave bands to obtain complete wavelength coverage, in some cases going from the radio to the X-ray of a variety of extragalactic objects. Although the apertures through which such broadband spectra are taken vary from wave band to wave band, the data have been chosen from the literature so as to minimize the difference in aperture size. There are some notable exceptions, such as *IRAS*, which has only a very large aperture. However, there is evidence in Calzetti et al. (1995) that the *IRAS* and the *IUE* fluxes of starburst galaxies are well correlated regardless of the large difference in the aperture of the two satellites, implying that the differences in this case may be minimal.

We have produced a plot comparing a normal S0 galaxy with a starburst galaxy, a Seyfert 2 galaxy, a template radio-quiet quasar, and a template radio-loud quasar. The SEDs shown in Figure 5 are from Sanders et al. (1989, the radio-loud and radio-quiet quasars), from Kinney et al. (1993, the UV spectra of the starburst, Seyfert 2, and S0 galaxies), from Weedman et al. (1981) and Israel & van der Hulst (1983, the radio and X-ray data on NGC 7714), from Ulvestad & Wilson (1984), Condon et al. (1982), and Pedlar et al. (1983, the radio data on NGC 1068), from Lawrence & Elvis (1982, the X-ray data on NGC 1068), from the *IRAS* Point-Source Catalog (the far-IR data for NGC 1068, NGC 1553, and NGC 7714), from Roche et al. (1991, the near-IR data for NGC 1068 and NGC 7714), from Fabbiano, Kim, & Trinchieri (1992, X-ray data on NGC 1553), from Subrahmanya & Harnett (1987, radio data on NGC 1553), and from Sadler (1984, radio data on NGC 1553).

To make a comparison between the SEDs of normal galaxies and galaxies with some activity, the starburst, Seyfert 2, and S0 galaxies are normalized in the red, at 1.2 μm, thus normalizing by their old star population. The Seyfert 2 galaxy shows little evidence for a hot star component such as dominates the starburst galaxy in the UV at log $v = 15.5$. However, the spectrum of the Seyfert 2 galaxy flattens out in the UV as the featureless blue continuum begins to dominate over the UV flux from the galaxy. The S0 galaxy shows a steeply decreasing UV flux, indicative of the lack of a hot star component. The X-ray flux of the Seyfert 2 galaxy is dominated by the active nucleus, with a UV–to–X-ray slope similar to that of the radio-loud and the radio-quiet quasars, while the lower relative X-ray flux of the starburst galaxy is most likely dominated by supernovae from the hot star population. The X-ray flux of the S0 galaxy is likely from a hot gaseous halo and, possibly, binary X-ray sources (Fabbiano 1989; see also Bregman, Hogg, & Roberts 1995).

In the *IRAS* bands, the Seyfert 2 galaxy shows strong emission from a hot dust component (≈ 500 K), while the starburst galaxy has stronger emission from the warm dust component (≈ 40 K; see also Calzetti et al. 1995). The S0 galaxy lacks the UV radiation to heat the dust to temperatures as high as those seen in the starburst galaxy and
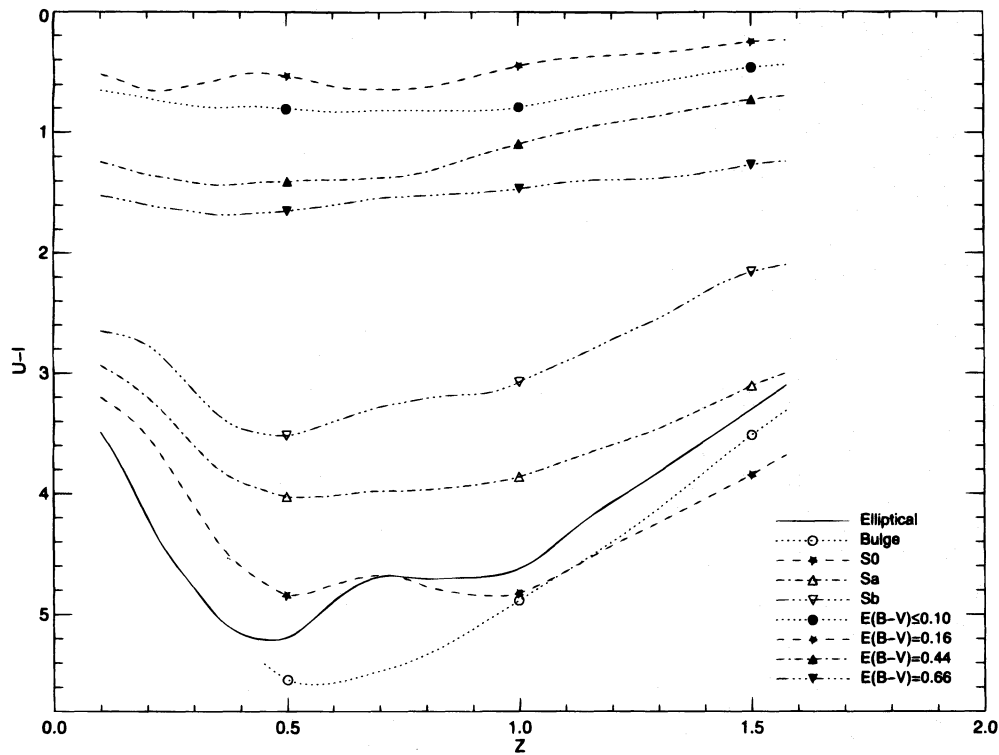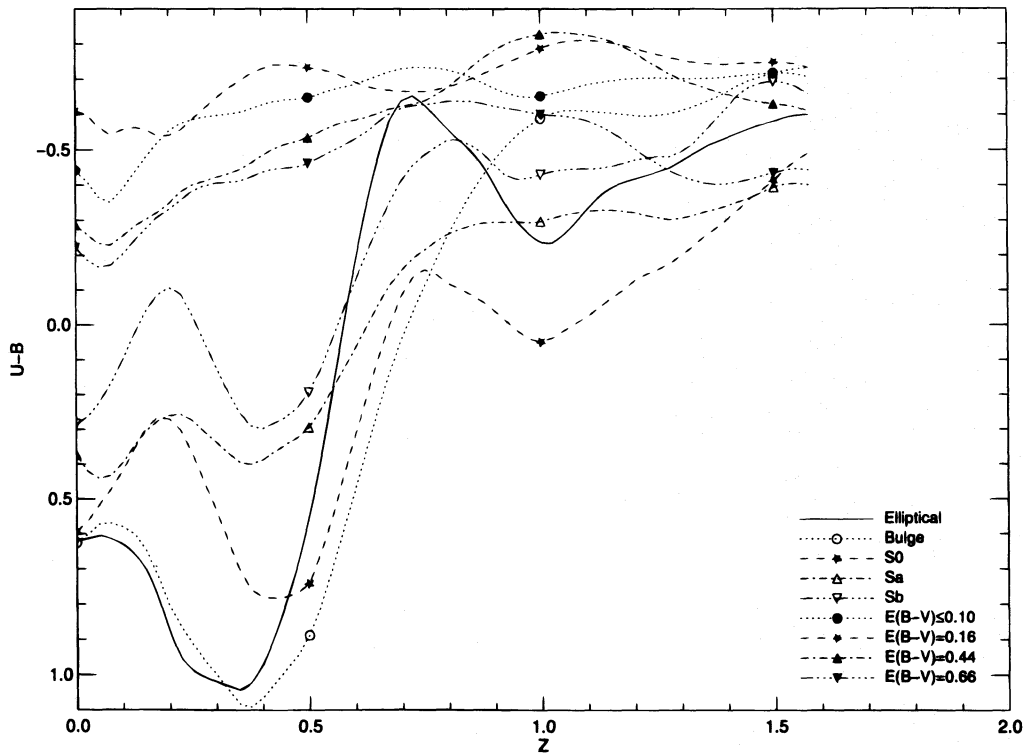
FIG. 3a

FIG. 3b

FIG. 3.—(a) Color $(U-I)$ vs. redshift for the template galaxies. (b) Color $(U-B)$ vs. redshift for the template galaxies.

therefore has weak emission in the *IRAS* wave bands.

The choice of the normalization between the galaxies' SEDs seems straightforward; the normalization in the near-IR, where the spectrum is dominated by old stars, simply allows a comparison by the mass of the galaxies. The choice of a normalization between the Seyfert 2 and the quasars is more of a best guess about how to compare the SEDs for the two types of objects. To make the comparison between
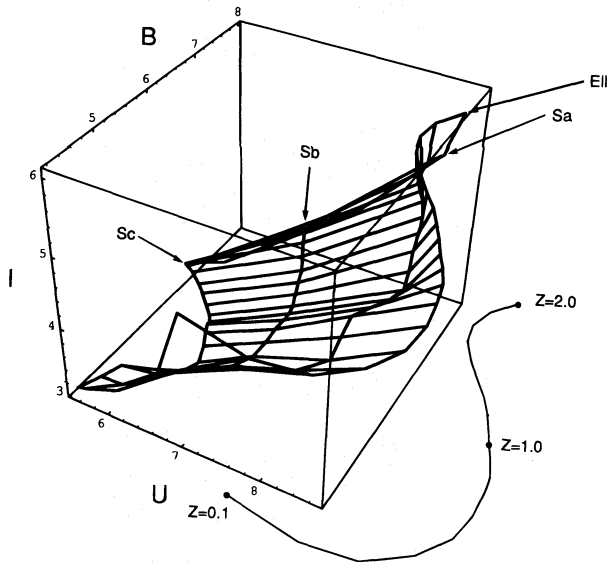
Fig. 4.—U, B, and I magnitudes are shown for the normal galaxy templates as a function of redshift, from $z = 0$ to $z = 2$. The grid shows the magnitudes for the elliptical, Sa, Sb, and Sc templates as four lines defining a curved surface. Lines of equal redshift, in increments of 0.1, are drawn perpendicular to the four lines. The galaxies have been normalized in the red. The curved line to the right of the cube shows the path of the elliptical galaxy template with redshift $z = 0.1$, $z = 1.0$, and $z = 2.0$ marked.

the dusty torus in active galaxies (Pier & Krolik 1992) shows that the flux between 60 and 100 μm is from the torus and is almost independent of the viewing angle of the torus. So the torus' contribution to the far-IR is isotropic, and a normalization at those far-IR wave bands should be a normalization to the size of the dusty torus. As long as we do not include blazars and BL Lac objects, there should be no further beamed contribution at the far-IR in the active objects (Antonucci 1993). Optical, UV, and X-ray bands are not suitable for the normalization, because they are dominated by a component that is dependent on the viewing angle (Antonucci 1993).

Several conclusions can be drawn from the SEDs of these extragalactic objects. First, the radio emission of the radio-quiet quasar is comparable to that of the starburst galaxy. Most likely, the radio emission of radio-quiet quasars is due to the star formation that accompanies activity in the center of the galaxy. Second, in the optical-to-UV region of the SEDs, the galaxies are only a factor of 10–100 fainter than the quasars. Thus, if the quasar's emission can be diminished by a factor of 100 with observing techniques (for example, by using the coronographic spot on NICMOS on the *Hubble Space Telescope*), the host galaxy SED should be readily observable. Finally, the red end of the optical spectrum is the best place to observe the host galaxy—before the big blue bump of the quasar begins to dominate the spectrum. However, based on the templates shown in Figure 1, the 4000 Å region is the region that most distinguishes between different galaxy types. Thus, the red spectral region, where the host galaxy is most readily observable, is not the same as the spectral region (4000 Å), where the host galaxy is most readily classifiable.
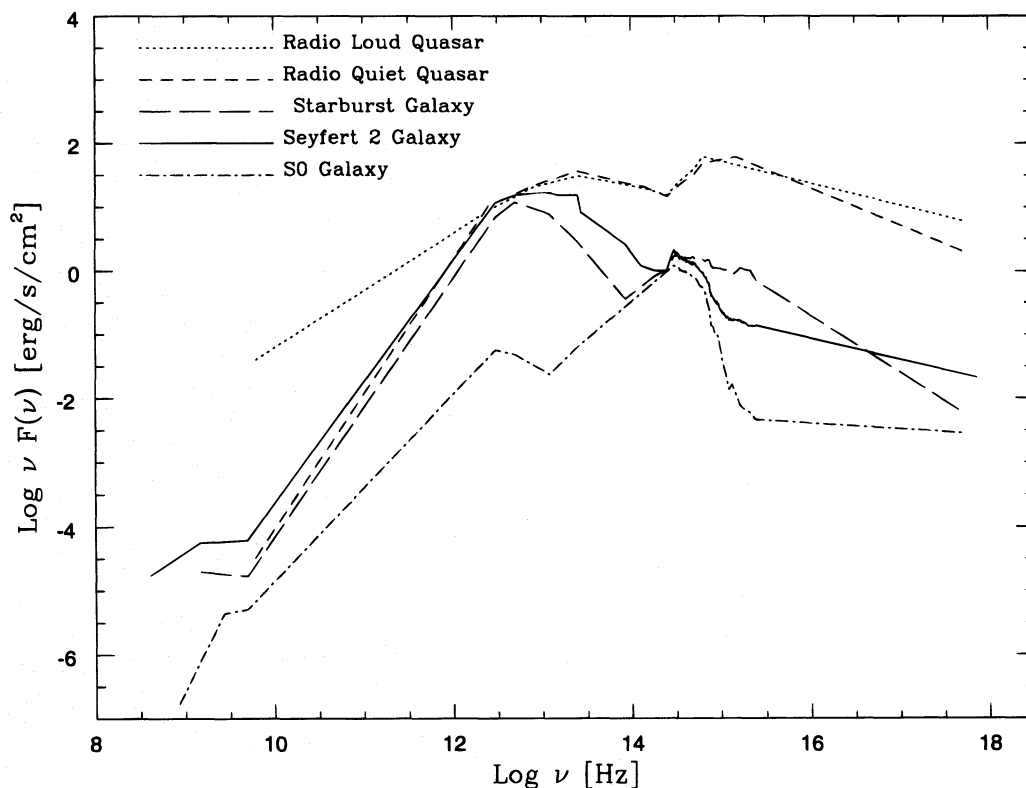
the Seyfert 2 galaxy, which has regions of its spectrum clearly dominated by the galaxy and regions clearly dominated by its active nucleus, and the quasars, we normalize the spectra at the $IRAS$ 60 μm band. Detailed modeling of

Fig. 5.—SED for the S0 galaxy NGC 1553, for the starburst galaxy NGC 7714, and for the Seyfert 2 galaxy NGC 1068 normalized at 1.2 μm, overlaid with a template radio-loud quasar and radio-quiet quasar from Sanders et al. (1989). The quasars are normalized to the Seyfert 2 galaxy by the flux in the $IRAS$ band at 60 μm, a flux that is thought to be isotropic and therefore not dependent on the orientation angle of the active nucleus.
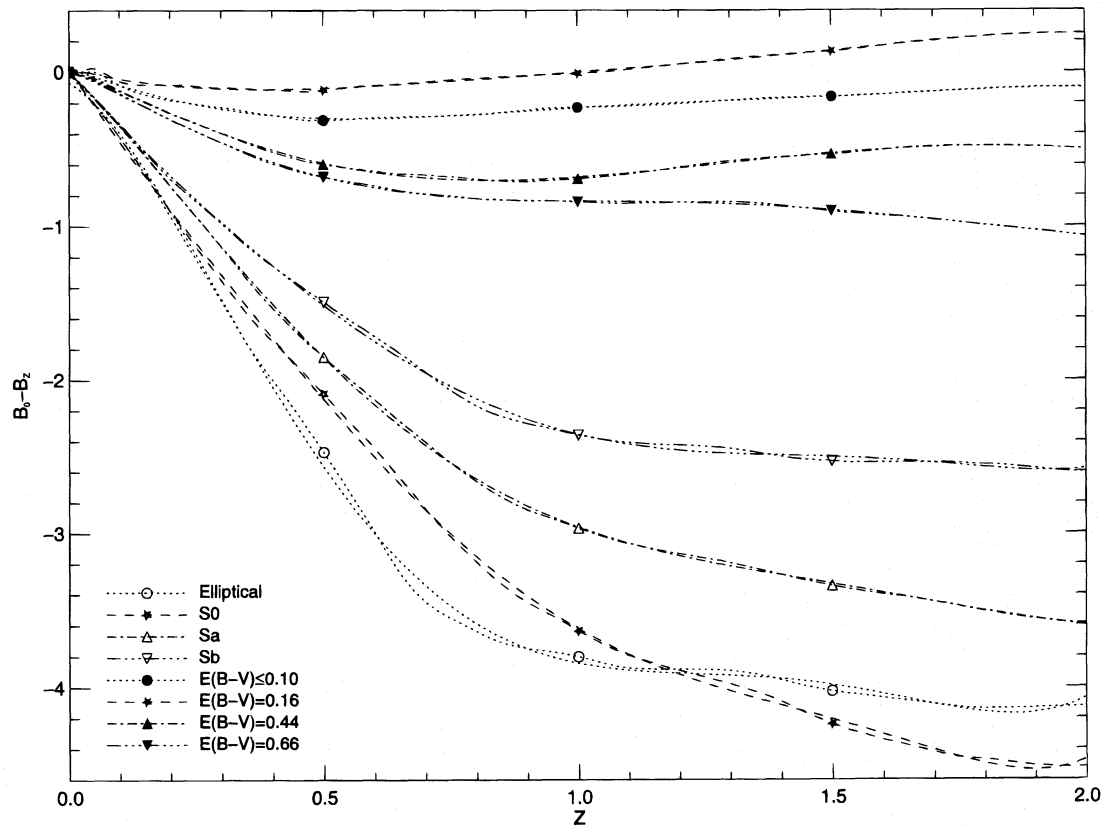
FIG. 6.—K-corrections [$B(z = 0) - B(z)$] as a function of redshift for the template galaxies. The polynomial fits are shown overlaid on the K-corrections. The fit parameters are given in Table 3.

4.4. K-Corrections and the Faint Galaxies' Number Counts

The number of faint blue galaxies detected in deep surveys (e.g., Koo & Kron 1982; Broadhurst, Ellis, & Shanks 1988) exceeds the number predicted from no-evolution models, typically based on the K-corrections[7] of Pence (1976) and Coleman, Wu, & Weedman (1980). The deviation of the number counts from the no-evolution hypothesis has been used to postulate various theories for the galaxy evolution. Indeed, more drastic processes than the passive evolution of the galaxy stellar populations are required in order to explain the excess in number counts, although the redshift distribution appears to be in remarkable agreement with the no-evolution hypothesis (for a review, see Koo & Kron 1992).

This section discusses the effect of the K-corrections on the expected number counts. While the Pence (1976) and Coleman et al. (1980) K-corrections were the best available for many years, as evidenced by their continuous use, the corrections are based on an inhomogeneous sample of UV and optical spectral data of galaxies, in order to reach a redshift of $z = 1.4$. Our template spectra match aperture size and morphological type with, typically, five galaxies

contributing to the UV spectral range and three of the same galaxies contributing to the optical spectral range (see Table 2), reaching a redshift of $z = 2.0$ for some bandpasses. Thus, these are self-consistent templates that can be used to calculate more accurate K-corrections as a function of redshift than previously available. These K-corrections can be used for a number of applications, including predictions of the number of faint blue galaxies as a function of magnitude. The K-corrections have been fitted to sixth-order polynomials and are shown as a function of redshift in Figure 6. The constants for the fits are given in Table 3. Our K-corrections for the bulge and E/S0 galaxies are similar to previous K-corrections (e.g., King & Ellis 1985 based on Pence 1976 and Coleman et al. 1980), but we also have a large dispersion of slopes as a function of morphological type, all the way to an almost constant value for the very blue starburst galaxies.

To evaluate the faint blue galaxies' number counts, we invoke assumptions similar to those used by Broadhurst (1989) and start with a mix of galactic morphological types based on the Durham/Anglo-Australian Redshift Survey (DARS, Broadhurst et al. 1988), but with an added starburst component. We assume a mixture of galaxies with 24% E/S0, 19% Sa, 23% Sb, 29% Sc–Sd, and 5% starbursting galaxies. We assume a Schechter (1976) luminosity function, given as

[7] The commonly used term K-correction originated as a reference to the K-term by Wirtz (1918), where K stands for the German word for constant, *konstante*. The K-term was a constant offset in redshift applied to "diffuse nebula," which were found to be receding, on average, by a velocity of 656 km s^{-1}. The average recession velocity was originally interpreted as local motion.

$$\phi(L)dL = \phi_* \left(\frac{L}{L^*}\right)^\alpha e^{(-L/L^*)}dL ,$$

TABLE 3

Polynomial Fits to K-Corrections:

$$B(0) - B(z) = K + Az + Bz^2 + Cz^3 + Dz^4 + Ez^5 + Fz^6$$

Type	K	A	B	C	D	E	F
Elliptical	−0.06592	−1.94619	−15.56946	25.90334	−15.81747	3.92798	−0.2762
Bulge	0.00042	−4.31986	−1.21184	−4.50550	11.33809	−6.92851	1.33613
S0	0.03107	−5.09886	3.87624	−8.89221	11.23979	−5.85310	1.07485
Sa	0.01013	−3.30775	−3.17835	6.07455	−2.97560	0.37363	0.04352
Sb	0.00782	−3.70729	2.21292	−3.65696	5.01346	−2.72938	0.50556
Sc	−0.00768	1.32313	0.58448	−16.14859	22.05992	−10.98042	1.89501
SB1	0.02797	−1.18577	0.62820	1.96862	−2.81187	1.37572	−0.23526
SB2	0.02841	−0.89573	1.87564	−1.46486	0.45232	0.03481	−0.03324
SB3	0.04050	−2.34058	5.26435	−5.52641	3.00158	−0.8093	0.08468
SB4	0.02050	−1.36718	−0.86146	3.48411	−2.76431	0.92692	−0.11951
SB5	0.00632	−1.38520	0.79897	1.32753	−1.91255	0.83166	−0.12048
SB6	0.01428	−1.44780	−1.65970	5.62661	−4.96270	1.84530	−0.25320

Notes.—SB1 refers to starburst galaxies with color excess $E(B-V) \leq 0.1$. SB2 refers to starburst galaxies with color excess $0.11 \leq E(B-V) \leq 0.21$. SB3 refers to starburst galaxies with color excess $0.25 \leq E(B-V) \leq 0.35$. SB4 refers to starburst galaxies with color excess $0.39 \leq E(B-V) \leq 0.50$. SB5 refers to starburst galaxies with color excess $0.51 \leq E(B-V) \leq 0.60$. SB6 refers to starburst galaxies with color excess $0.61 \leq E(B-V) \leq 0.70$.

where $\alpha = -1.25$. Following the methodology of Broadhurst (1989), we use the mean absolute B_j magnitude for the galaxies in the DARS to set $M^* = -2.5 \log L^* + $ const for each galaxy type:

E/S0: $M^* = -21.6 + 5 * \log (H_0/100.)$,

Sa/Sb: $M^* = -21.15 + 5 * \log (H_0/100.)$,

Sa/Im: $M^* = -20.85 + 5 * \log (H_0/100.)$,

starburst: $M^* = -19.65 + 5 * \log (H_0/100.)$,

and we use our derived K-corrections to predict the number counts. The number counts as a function of the apparent magnitude m are given by

$$N(m) = 4\pi \left(\frac{c}{H_0}\right)^3$$

$$\times \int_0^\infty \frac{[q_0 z + (q_0 - 1)(\sqrt{1 + 2q_0 z} - 1)]^2}{q_0^4 (1 + z)^2 \sqrt{1 + 2q_0 z}} \, dz$$

$$\times \int_{L(z)/L^*} \phi(L) dL \,,$$

with

$$\frac{L(z)}{L^*} = \left[\frac{D(z)}{D(z^*)}\right]^2 10^{0.4[k(z) - k(z^*)]} \,,$$

where $k(z)$ is the K-correction.

Our prediction of number counts in the case of no galaxy evolution, shown as a solid line in Figure 7, underpredicts the observed number counts as reported in Broadhurst et al. (1988). Our predictions are practically indistinguishable from those based on the Pence (1976) data (Fig. 7, dashed line) and show that the number counts are not greatly sensitive to variations in the K-corrections (see also King & Ellis 1985).

As a simple experiment, we also calculate a prediction based on the hypothetical galaxy mixture made up of 100% mildly reddened starburst galaxies. We find that a population made up entirely of starbursting galaxies with

reddening $E(B-V) \sim 0.3$, given by the dot-dashed line in Figure 7, is compatible with the number counts.

4.5. Comparison of Templates with Stellar Synthesis Models

How do the observed templates compare with the SEDs computed in spectral synthesis programs? We make comparisons here for the populations representing the extremes in ages: the elliptical galaxy and the bluest starburst galaxy.

In Figure 8, we overlay the template for the elliptical galaxy (solid line) with the best matching synthetic spectrum (dotted line) based on the Bruzual & Charlot (1993) code. We use the model of a single instantaneous burst with an age of 16 Gyr. The spectra have been normalized at 4000 Å. The model and the template show similar features in general, with the size of the 4000 Å discontinuity, the most marked feature in the template, being well matched. There is some mismatch at the red end of the spectrum, which may
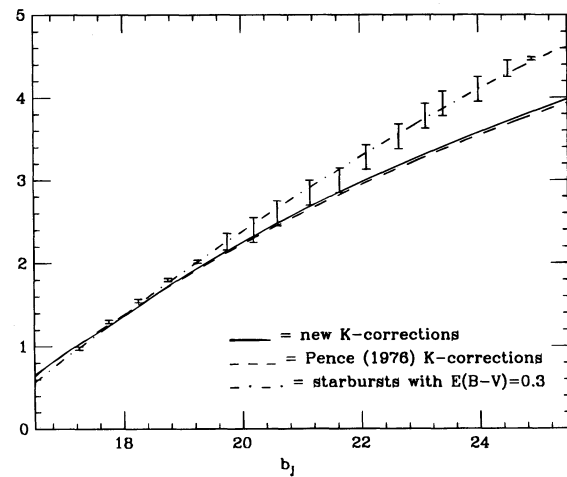

Fig. 7.—Prediction for number counts for the no-evolution galaxy model compared with the data of Broadhurst et al. (1988) as a function of the blue magnitude B_j. Data are given with 1 σ error bars. Prediction based on our K-corrections are given by the solid line. Predictions based on Pence (1976) K-corrections are given by the dashed line. For comparison, a prediction based on a highly unphysical universe made up completely of starbursts with low dust content is given by the dot-dashed line.
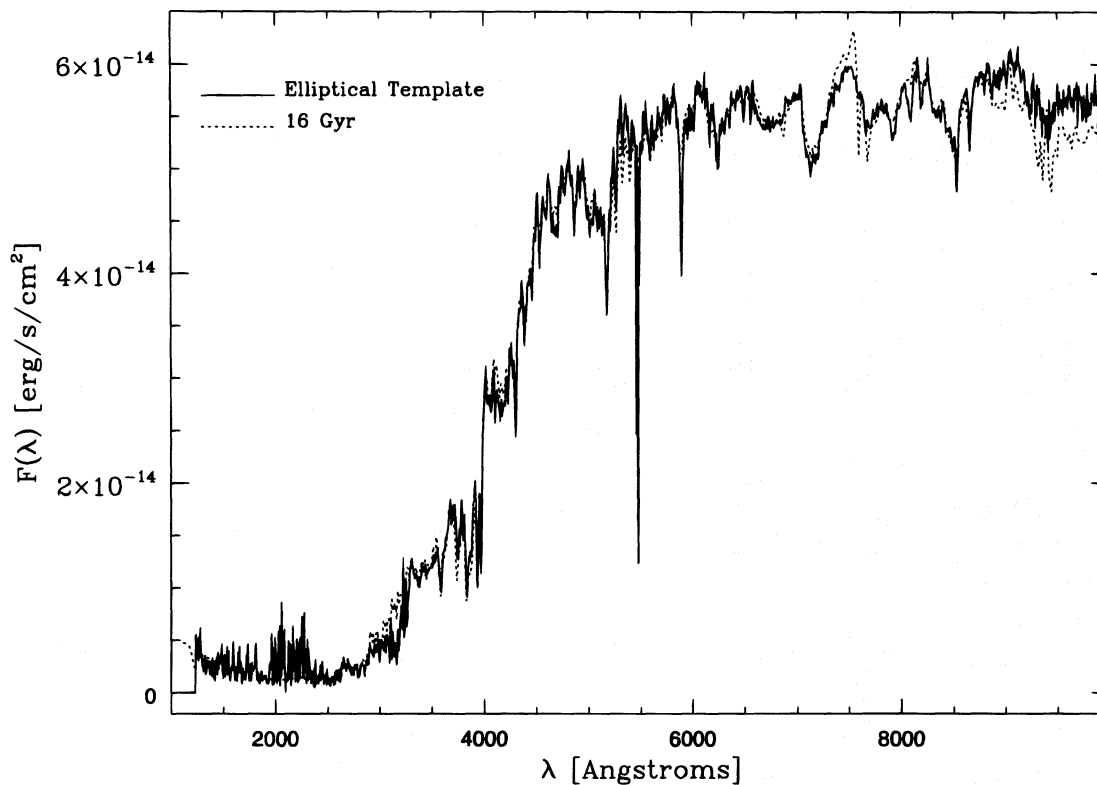
FIG. 8.—The elliptical template (*solid line*) is plotted with a synthetic spectrum overlaid (*dotted line*). The spectra are normalized at 4000 Å. The synthetic spectrum is based on a single burst model of age 16 Gyr.

be attributed to the ongoing developments in understanding the properties of the low end of the initial mass function (Charlot, Worthey, & Bressan 1996).

Figure 9 shows our starburst template for the case $E(B-V) = 0.0$ (*solid line*) overlaid with a synthetic spectrum (*dashed line*) based on a Bruzual & Charlot (1993) model using continuous star formation and an age of 7.2×10^8 yr, and normalized at 4000 Å. Since Bruzual & Charlot models to not include nebular emission, the emission lines are lacking in the synthetic spectrum. The continuum match is nonetheless fairly good in the optical and in

the long-wavelength end of the UV. The major difference between the two spectra is at wavelengths shorter than 2000 Å, where the template is markedly redder than the synthetic spectrum. The most likely explanation for the difference is that the template spectrum includes star-forming regions of different ages and different dust content, while the synthetic spectrum includes only one dust-free region undergoing continuous star formation (cf. Leitherer & Heckman 1995). However, for actual comparisons with high-redshift galaxies, the observed templates may be a more realistic version of a "starburst galaxy" than the models.
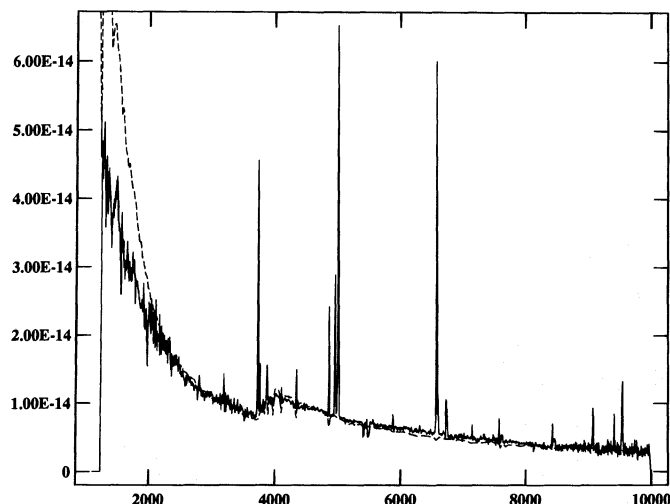
FIG. 9.—The template for the starburst galaxy (*solid line*) with $E(B-V) = 0.0$ is plotted with a synthetic spectrum overlaid (*dashed line*). The spectra are normalized at 4000 Å. The synthetic spectrum is based on a continuous star formation model of age 7.2×10^8 yr.

5. CONCLUSIONS

We present template UV-optical spectra of quiescent and starburst galaxies, from a combination of *IUE* data and of optical data with an aperture size matched to the *IUE*. The templates are built according to morphological type for the quiescent galaxies and according to color excess for the starburst galaxies (cf. Calzetti et al. 1994). Comparison of our templates with Kennicutt's (1992) large-aperture optical spectra suggests that, despite our relatively small observational apertures, the galaxy stellar populations are well represented in the elliptical, S0, Sa, and Sc templates. The relatively young disk stars are underrepresented relative to the old bulge population in our Sb template. Starburst galaxies are dominated by the central burst of star formation, which is well sampled by our spectra.

Analysis of galaxy colors shows that colors do not generally help to define a detailed morphological classification of a galaxy or to determine its redshift. However, the magnitudes of the galaxies in multiple wave bands do separate the galaxies both by morphological type and by redshift, so that three-dimensional "magnitude cubes" should provide a useful tool in identifying distant galaxies (Connolly et al. 1995).

The spectra of an S0 galaxy, a starburst galaxy, and a Seyfert 2 galaxy are joined with data from the literature to form multifrequency spectra spanning the range from radio to X-ray. These spectra are displayed together with template active galaxies, allowing a comparison over a wide spectral range. In addition, the reddest (elliptical) template and the bluest ("dust-free" starburst) template are compared with stellar synthesis models. There is a general satisfactory agreement between models and templates; the major difference is in the far-UV side of the starburst spectra and can be attributed to the presence of more than one region of star formation contributing to the integrated emission.

Template spectra are used to calculate K-corrections for galaxies as a function of morphological type and redshift, up to $z \simeq 2$. Despite the fact that these K-corrections are a clear improvement over previous determinations (cf. King & Ellis 1985; Broadhurst et al. 1988), the blue galaxy number counts they predict in the case of no-evolution are not very different from the number counts predicted by previous K-corrections. Improved K-corrections do not help resolve the anomalously high number of faint blue galaxies detected by deep surveys (cf. King & Ellis 1985).

APPENDIX

We have derived color-color and color-versus-redshift diagrams using the standard Johnson bandpasses U, B, V, R, and I, shown as response versus log ν in Figure 10, and the bandpasses developed by Steidel & Hamilton (1992, 1993) specifically for searching for high-redshift galaxies (U_n, G, and $\mathscr{R}$, shown in Fig. 11). For comparison purposes, the energy distributions of the quiescent galaxy templates are plotted in Figure 12, and the energy distributions of the starburst templates are plotted in Figure 13 as νF_ν versus log ν. The quiescent galaxies have only one noticeable feature, the strong 4000 Å discontinuity, while the starburst galaxies show a slight increase in flux across the 4000 Å discontinuity.

Table A1 lists the template fluxes, normalized by averaging between 3800 and 4200 Å to the bulge spectrum for comparison between the templates. The table lists the mean in each 200 Å bin in units of 1×10^{-14} ergs cm^{-2} s^{-1} Å^{-1}, and the standard deviation in the fluxes in the corresponding bin in the same units.

The color-versus-redshift diagrams and color-versus-color diagrams for the different morphological types at different redshift are shown in Figure 14.
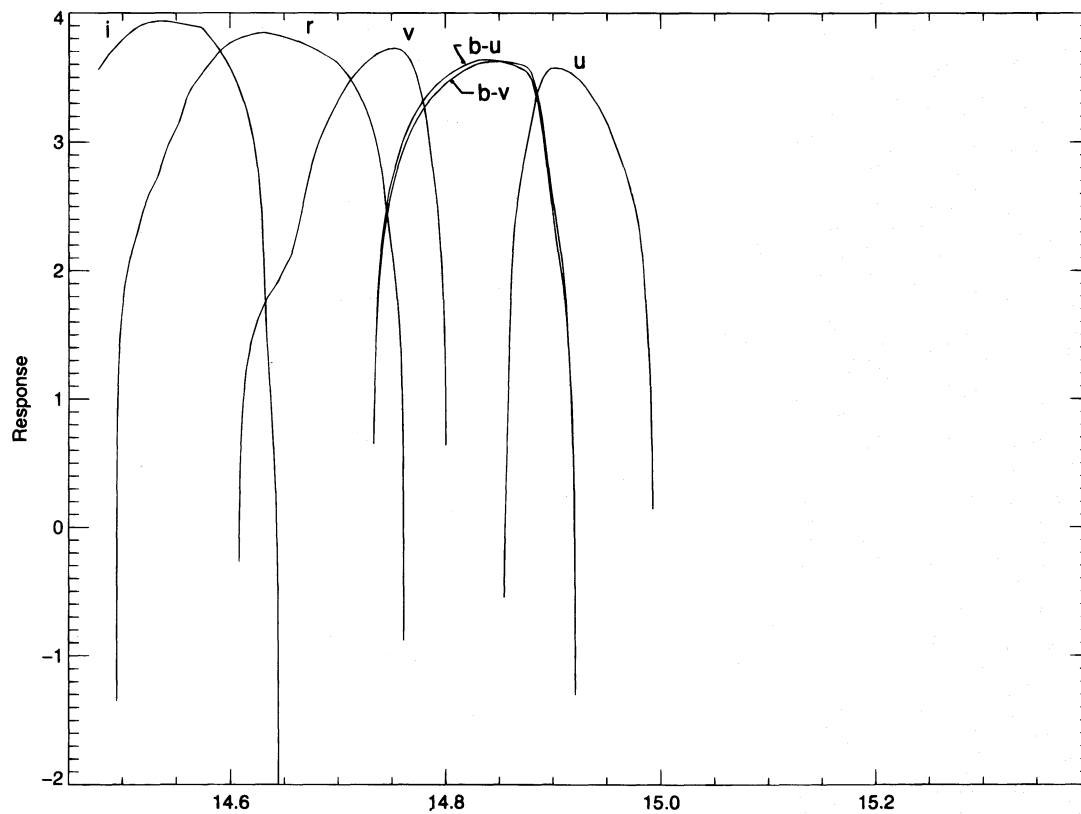
FIG. 10.—Standard bandpasses *U*, *B*, *V*, *R*, and *I* are shown with the bandpass response plotted vs. log *v*
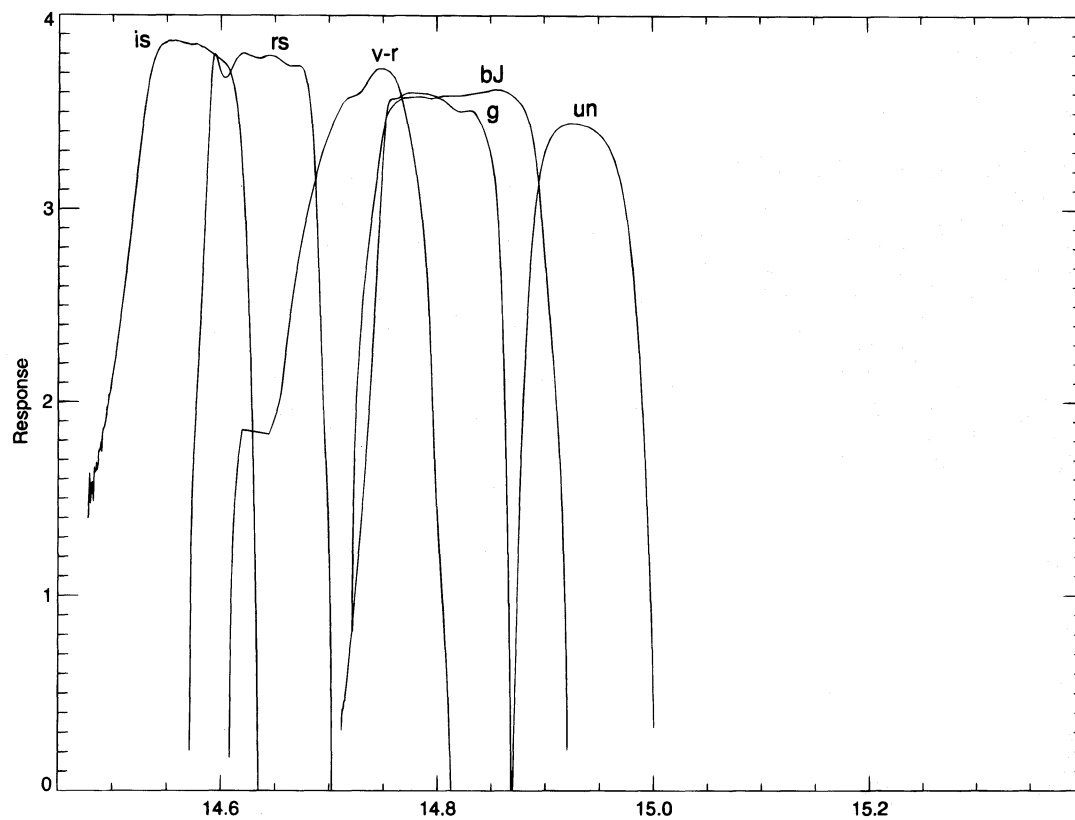
FIG. 11.—Special bandpasses developed by Steidel & Hamilton (1992, 1993). U_n, *G*, and $\mathscr{R}$ are shown with the bandpass response plotted vs. log *v*.

FIG. 12.—Templates of normal galaxies plotted in the same units as Figs. 10 and 11

FIG. 13.—Templates of starburst galaxies plotted in the same units as Figs. 10 and 11

53

FIG. 14.—Color vs. redshift and color vs. color for the template spectra using the bandpasses shown in Figs. 10 and 11

FIG. 14—*Continued*

Fig. 14—*Continued*

56

FIG. 14—*Continued*

57
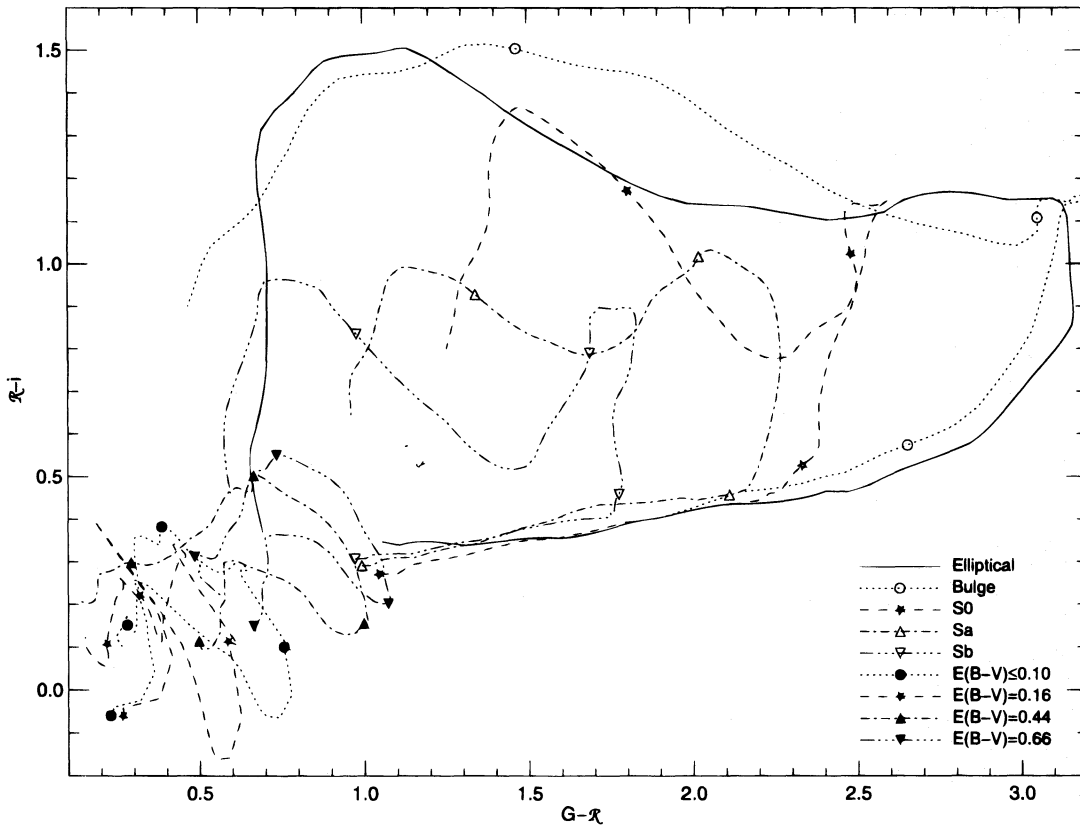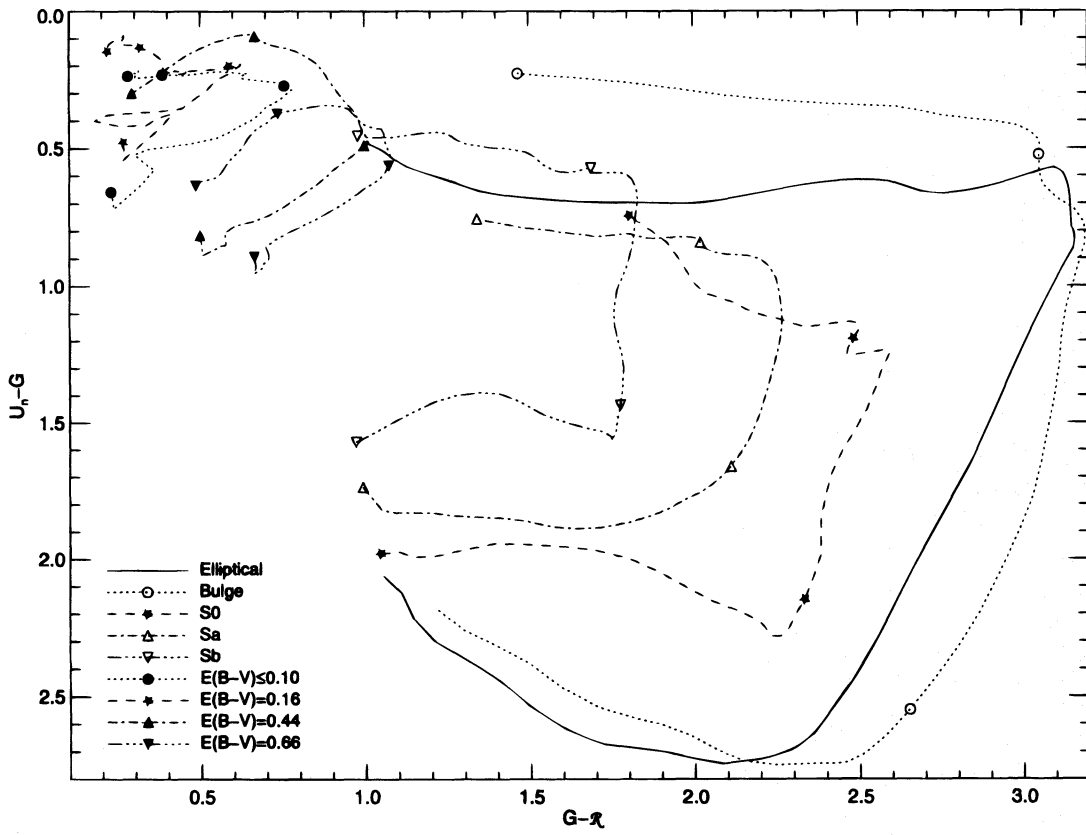
Fig. 14—*Continued*

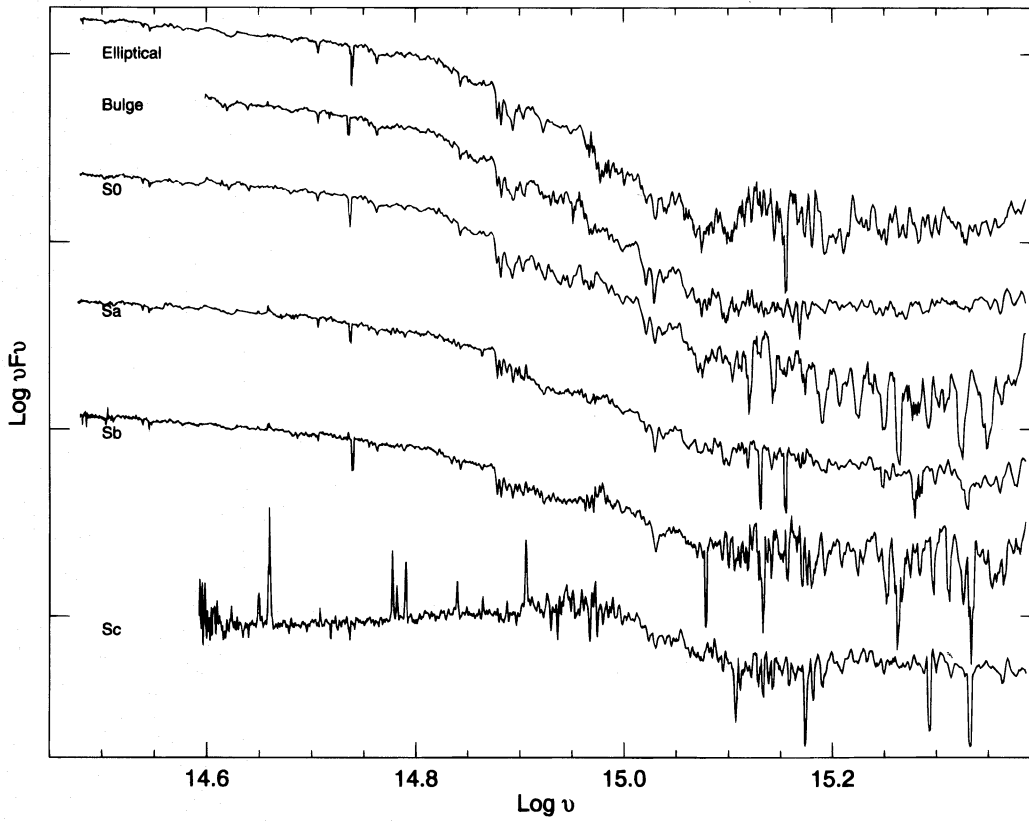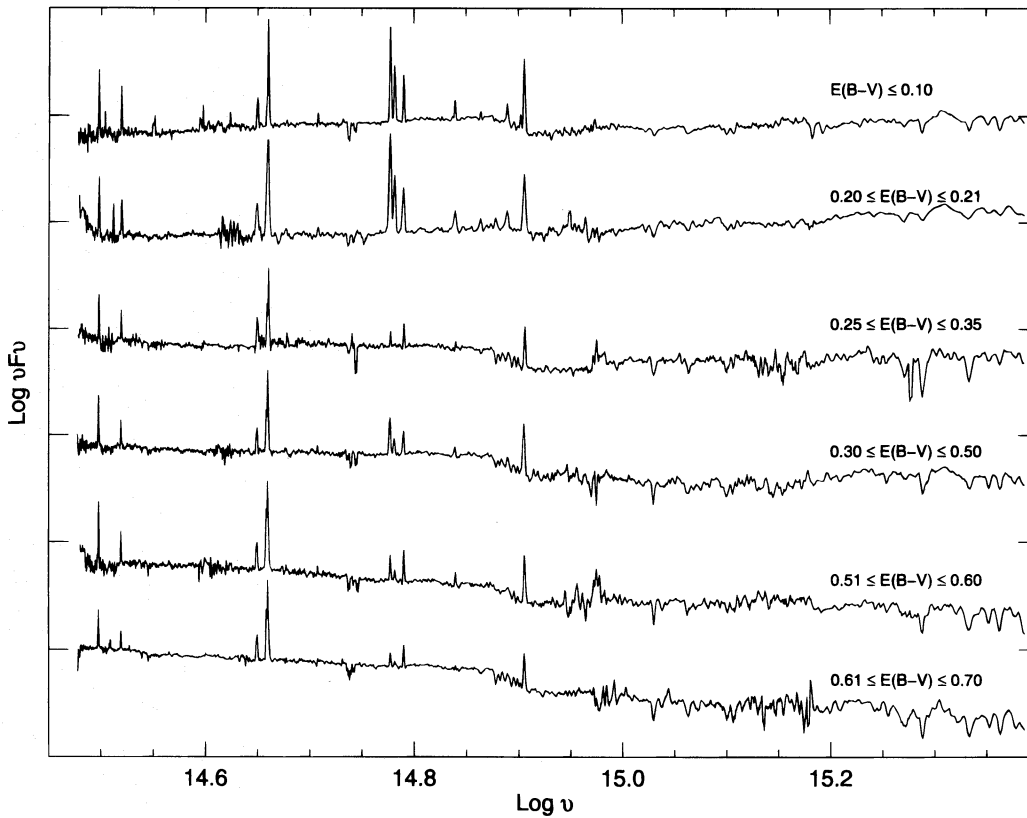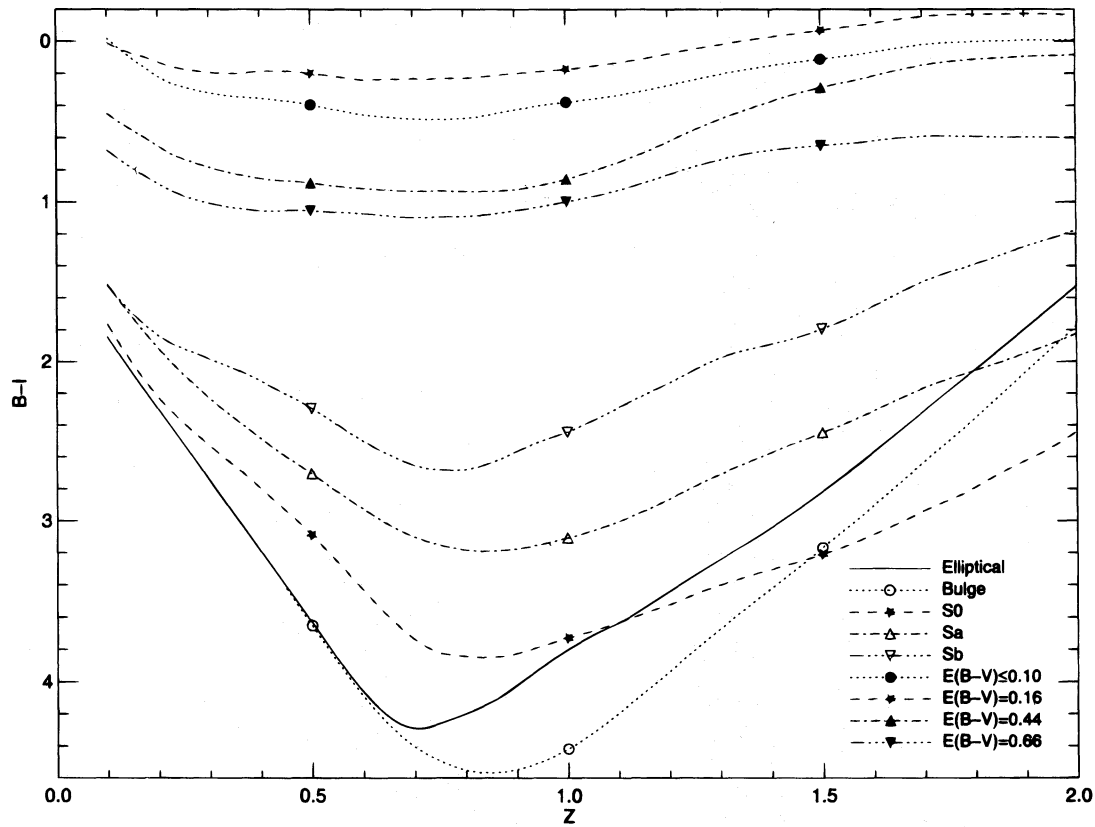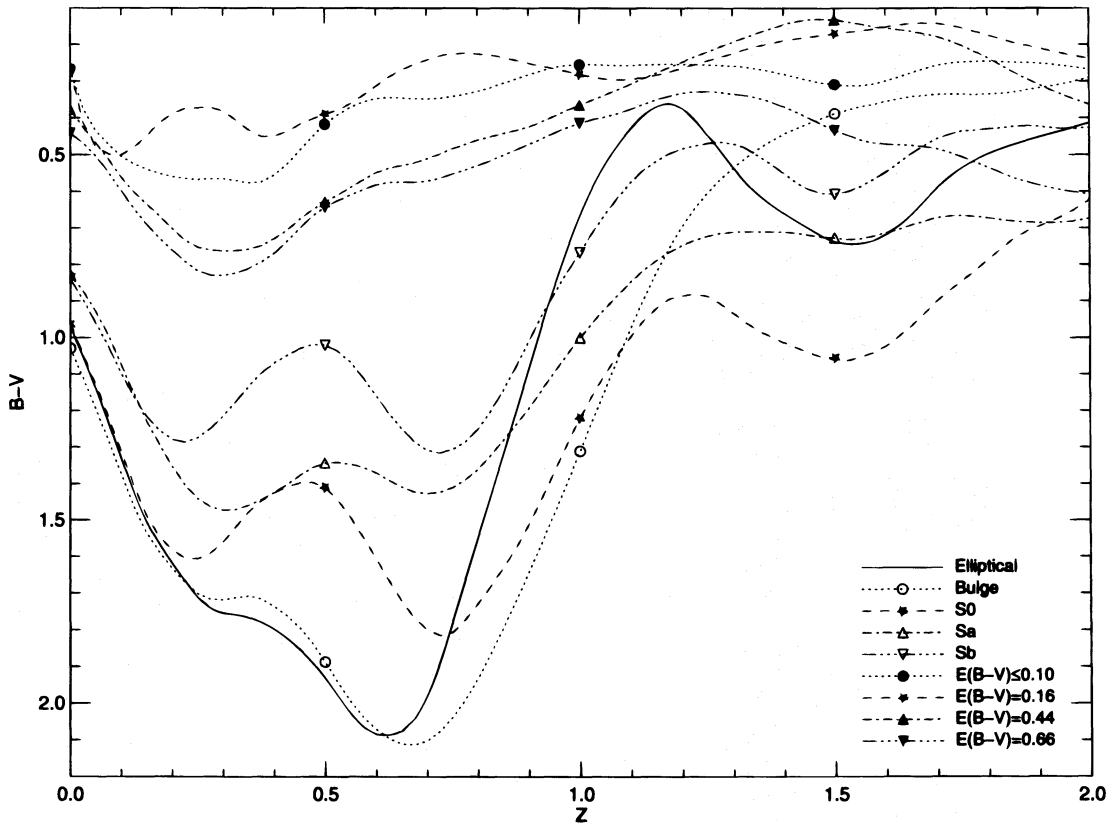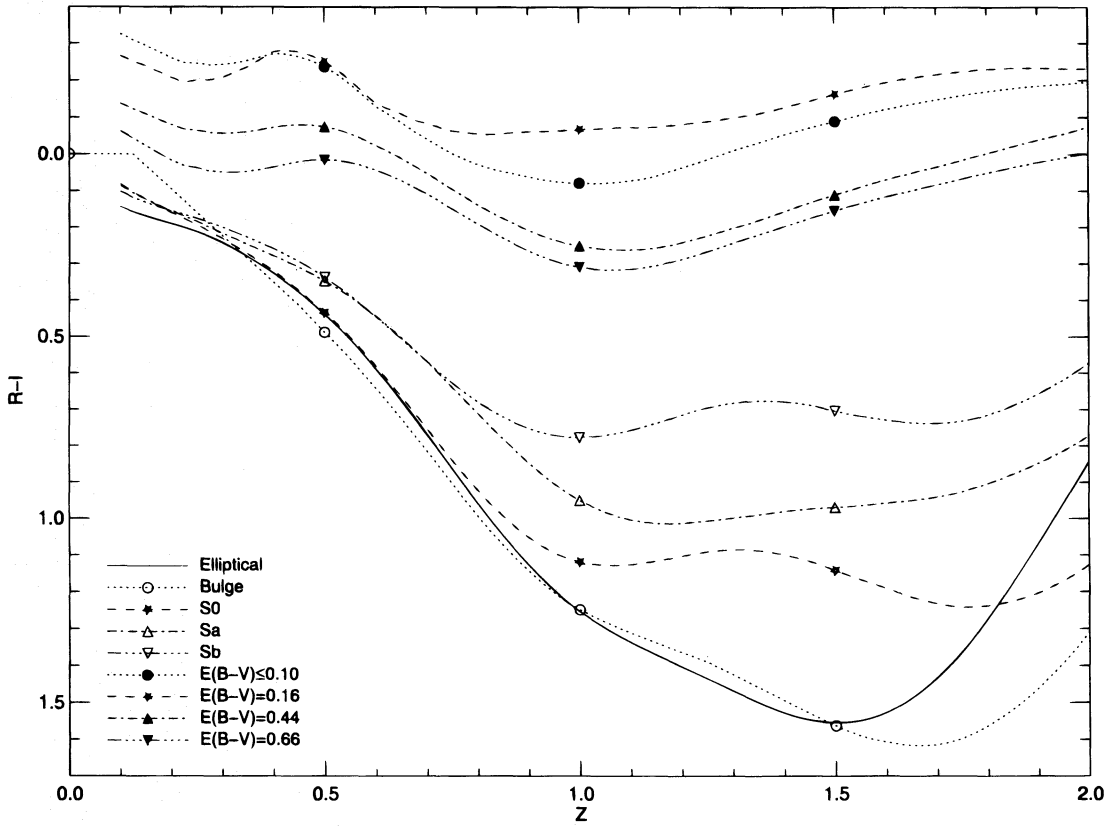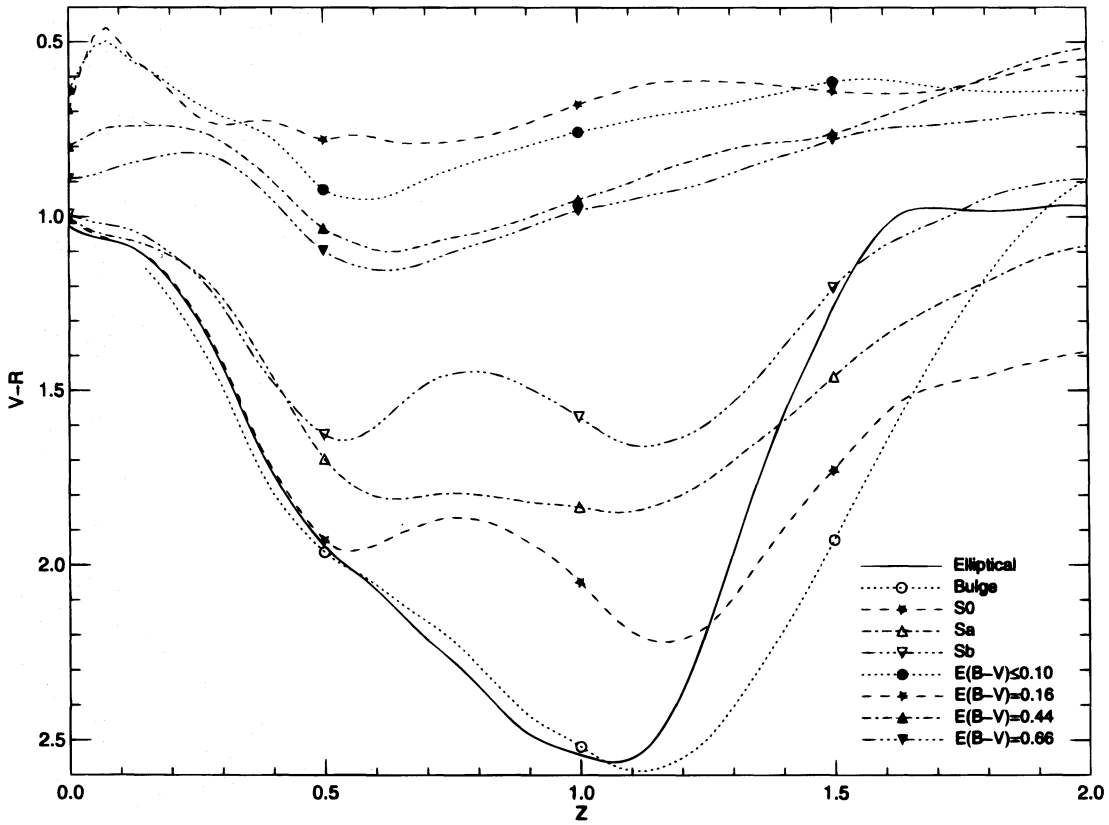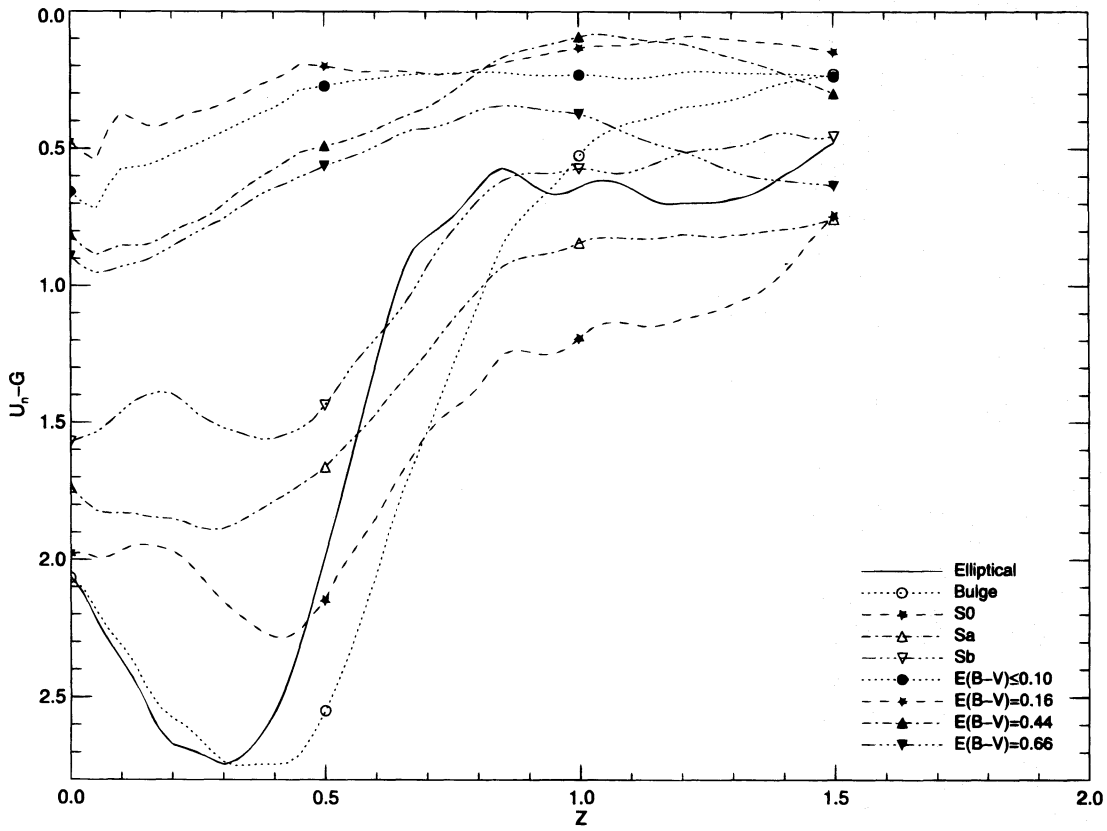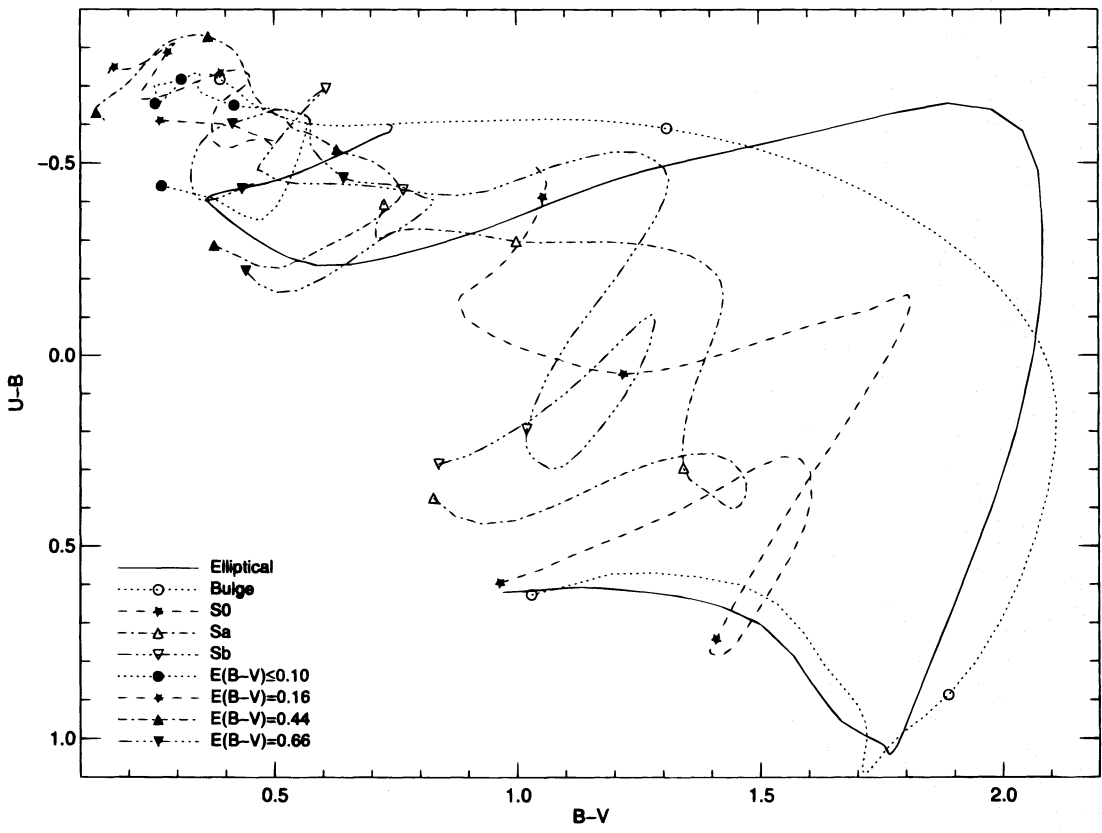|	Ellip	Bulge	S0	Sa	Sb	Sc	SB1	SB2	SB3	SB4	SB5	SB6
1100–1300	2.832	2.092	2.417	2.917	8.426	11.679	46.109	64.090	44.953	30.550	26.416	17.169
	0.704	0.351	1.496	0.779	3.773	2.688	3.450	5.691	5.807	3.249	4.680	2.933
1300–1500	1.791	1.602	1.197	2.111	6.081	11.219	42.371	58.913	38.396	29.283	24.971	16.591
	0.501	0.243	0.761	0.568	3.377	2.794	4.479	5.160	5.739	3.615	4.186	3.039
1500–1700	1.610	1.245	1.118	2.048	4.911	10.810	34.954	47.182	30.297	25.717	22.577	15.611
	0.612	0.253	0.856	0.624	2.802	3.128	3.340	4.823	7.968	3.349	3.684	2.855
1700–1900	1.440	1.181	1.197	2.340	5.281	10.846	29.961	41.502	31.338	23.890	22.772	17.026
	0.636	0.137	0.632	0.286	1.659	2.274	2.707	3.382	3.829	2.582	2.131	1.763
1900–2100	1.726	1.012	1.456	2.397	4.954	7.500	26.654	31.801	24.977	18.498	21.287	15.367
	1.220	0.242	0.902	0.529	3.076	2.897	3.004	3.942	6.024	2.855	3.303	4.765
2100–2300	1.950	0.970	2.025	2.526	5.029	7.734	23.738	28.124	22.384	15.336	21.350	14.117
	1.146	0.259	1.170	0.801	3.098	3.171	2.503	2.169	6.891	2.423	3.341	3.503
2300–2500	1.166	0.925	1.623	2.508	4.216	7.902	20.348	26.188	21.296	14.335	17.419	11.972
	0.583	0.272	0.623	0.524	1.514	3.166	1.575	2.708	3.290	1.966	2.537	2.091
2500–2700	1.257	1.290	2.051	2.925	4.361	10.188	18.330	23.355	19.069	13.194	16.314	11.765
	0.508	0.428	0.797	0.594	1.170	2.372	0.956	1.875	2.022	1.330	1.595	1.270
2700–2900	1.622	1.635	2.917	3.437	5.412	12.161	16.617	20.447	17.545	12.248	14.820	11.636
	0.391	0.408	0.718	0.609	1.245	2.075	0.931	2.345	1.872	1.379	1.814	1.800
2900–3100	2.896	3.270	5.593	5.490	8.468	19.182	16.567	17.971	16.364	12.899	15.176	12.264
	0.431	0.357	0.7505	0.553	1.024	3.753	0.683	1.650	1.403	0.953	1.222	1.858
3100–3300	4.544	4.882	7.735	6.822	10.562	22.048	15.253	16.349	15.704	12.040	16.372	11.676
	1.827	1.318	1.558	0.988	2.497	8.585	1.451	4.033	4.149	2.457	5.290	2.254
3300–3500	7.771	8.331	7.914	7.266	9.095	22.522	13.056	17.422	12.073	12.724	13.046	11.453
	0.449	1.598	1.537	0.439	0.733	7.093	0.860	6.558	0.644	1.451	2.739	0.843
3500–3700	9.280	10.014	9.644	8.006	9.949	19.250	11.689	13.814	11.576	11.311	11.967	11.051
	1.498	1.684	1.730	0.901	1.206	3.875	0.628	1.877	0.584	0.977	0.959	0.520
3700–3900	9.879	9.603	9.702	10.711	10.923	22.638	17.406	19.186	14.000	14.765	14.423	13.741
	1.633	1.436	1.639	1.523	1.295	21.265	11.103	11.122	4.170	5.760	4.986	3.239
3900–4100	15.535	15.703	15.348	15.263	15.013	14.481	14.662	14.487	14.911	14.917	14.891	14.957
	4.416	4.241	4.716	3.141	3.439	1.513	0.653	1.363	1.393	1.162	0.942	1.376
4100–4300	19.544	19.331	19.771	17.780	18.315	14.368	14.342	13.354	15.508	15.493	15.228	15.466
	1.380	1.538	1.226	1.019	0.934	2.393	0.715	1.305	0.573	0.419	0.494	0.443
4300–4500	25.059	25.956	25.147	19.589	19.647	14.600	13.579	12.913	15.105	14.766	14.655	14.879
	2.977	3.076	3.144	1.352	1.787	4.274	1.810	2.256	0.931	0.843	1.250	0.489
4500–4700	30.729	32.016	30.548	22.151	23.399	12.302	12.714	11.588	15.083	14.612	14.961	15.211
	1.397	1.337	1.474	0.931	1.127	0.943	0.278	0.603	0.519	0.344	0.440	0.230
4700–4900	32.375	33.844	30.974	22.093	23.896	13.385	13.188	12.961	14.838	14.756	15.056	14.995
	1.385	1.099	1.340	1.068	1.117	8.690	4.686	5.718	2.385	2.203	3.452	1.973
4900–5100	31.707	33.842	31.464	22.262	23.821	14.631	19.569	23.689	14.074	15.238	14.843	14.216
	1.419	1.419	0.964	0.973	0.789	11.513	19.484	28.566	1.437	4.422	2.587	1.208
5100–5300	31.158	32.826	30.828	22.233	23.502	9.436	10.206	9.334	13.040	12.410	13.320	13.233
	3.053	2.999	2.540	1.131	1.514	0.676	0.264	0.664	0.591	0.388	0.469	0.341
5300–5500	33.890	38.709	34.236	23.290	24.129	8.824	9.282	8.481	12.154	11.606	12.431	12.438
	6.821	1.132	4.919	2.859	4.840	0.673	1.096	1.092	2.509	1.647	1.686	1.612
5500–5700	36.197	38.059	35.170	24.507	26.045	8.198	9.319	8.482	12.548	11.696	13.479	12.897
	0.892	5.271	4.457	1.876	1.504	1.194	0.694	0.698	0.537	0.755	0.566	0.786
5700–5900	36.708	40.492	35.924	25.708	26.962	8.141	9.173	8.481	12.524	11.625	13.729	12.947
	2.648	3.211	2.040	1.643	1.304	1.250	0.693	0.573	0.783	0.617	0.899	0.516
5900–6100	37.096	42.011	36.550	26.128	25.736	7.675	8.718	7.961	12.051	11.489	13.300	12.685
	1.926	1.791	1.836	0.942	1.073	0.623	0.220	0.453	0.850	0.475	0.759	0.324
6100–6300	36.920	40.526	35.822	25.842	25.367	7.193	8.334	7.707	11.833	10.885	13.372	12.358
	1.503	1.603	1.431	1.108	1.166	0.654	0.333	0.509	1.305	0.652	0.812	0.391
6300–6500	37.814	41.606	37.177	25.039	26.881	6.989	8.024	7.374	11.393	10.801	13.498	12.246
	0.857	1.096	0.991	0.959	0.544	0.491	0.372	0.822	0.999	0.524	0.774	0.411
6500–6700	37.655	42.740	37.297	26.781	27.287	17.392	13.323	16.671	15.920	15.922	23.199	18.622
	0.961	1.409	0.658	1.705	1.577	29.230	16.515	18.082	12.049	12.885	20.872	14.796
6700–6900	36.892	41.193	35.850	25.602	26.447	7.562	7.805	8.189	10.919	10.907	14.268	12.655
	0.426	1.802	1.417	0.519	0.627	2.597	2.065	2.708	3.061	2.231	3.349	2.777
6900–7100	37.814	42.473	38.121	25.682	26.781	6.121	7.048	7.033	9.710	9.852	12.635	11.751
	1.178	1.272	1.220	0.707	0.708	0.794	0.377	1.567	0.384	0.580	0.641	0.583
7100–7300	35.211	38.537	35.485	24.046	25.100	5.995	6.876	7.201	9.210	9.435	12.576	11.273
	1.094	1.821	2.017	0.580	0.570	1.438	0.820	2.527	0.249	1.243	1.140	0.212
7300–7500	39.055	43.891	37.513	25.898	26.873	7.050	6.743	6.542	9.395	9.643	12.377	11.564
	0.883	2.077	1.251	0.410	0.570	1.936	0.576	0.440	0.194	0.836	1.715	0.189
7500–7700	38.657	47.218	36.199	25.938	26.166	8.795	6.644	6.324	9.003	8.969	12.556	11.166
	1.391	1.598	2.485	1.031	0.652	5.103	1.260	0.292	0.578	0.439	1.520	0.383
7700–7900	37.453		34.125	25.094	25.872		5.764	6.277	8.851	9.015	12.143	10.870
	0.513		0.536	0.349	0.537		0.196	0.370	0.308	0.350	0.590	0.122
7900–8100	37.603		34.029	24.761	25.759		5.444	5.830	8.650	8.786	11.646	10.767
	1.131		1.055	0.618	0.780		0.171	0.285	0.251	0.368	0.670	0.243
8100–8300	39.211		34.882	25.510	26.335		5.233	5.716	8.691	8.892	11.703	10.651
	0.921		0.882	1.087	0.720		0.368	0.404	0.361	0.309	0.652	0.293

TABLE A1—*Continued*

	Ellip	Bulge	S0	Sa	Sb	Sc	SB1	SB2	SB3	SB4	SB5	SB6
8300–8500	37.009		33.167	23.091	25.231		5.331	5.404	8.336	8.514	11.340	10.218
	0.726		0.781	0.378	0.533		0.896	0.320	0.537	0.398	0.555	0.250
8500–8700	36.779		32.644	22.779	24.784		4.925	5.264	8.223	8.358	11.042	10.146
	1.852		1.980	1.183	1.690		0.304	0.352	0.481	0.511	0.963	0.576
8700–8900	39.623		35.158	24.340	26.399		4.913	5.381	8.748	8.639	11.319	10.758
	0.527		0.831	0.454	0.914		0.421	0.489	0.742	0.460	0.799	0.247
8900–9100	40.073		35.533	24.592	26.279		5.476	6.032	9.118	8.987	11.803	11.343
	0.708		0.950	0.543	0.722		2.104	2.226	1.980	1.693	2.823	1.401
9100–9300	39.241		34.490	23.501	25.652		4.357	5.464	8.104	8.177	9.900	10.767
	1.258		1.071	0.934	1.468		0.572	2.139	0.866	0.677	1.150	0.888
9300–9500	37.250		32.952	22.832	24.800		4.781	4.929	7.745	7.748	9.851	10.451
	0.958		1.549	0.741	2.663		1.172	0.769	1.478	0.693	1.215	0.783
9500–9700	38.234		33.678	23.230	25.012		5.418	6.731	9.349	9.449	11.961	11.529
	0.539		0.830	0.425	0.880		3.600	4.785	3.726	4.295	7.398	3.408
9700–9900	38.069		33.669	23.206	24.779		4.022	6.879	8.828	8.155	11.737	10.291
	0.681		0.762	0.401	1.977		0.754	1.498	1.111	1.036	1.973	0.588
9900–10000	36.476		33.537	22.898	24.257		3.975	8.041	9.219	7.557	13.070	9.036
	3.542		1.025	0.792	3.243		0.592	1.320	1.126	1.214	0.711	1.758

NOTE.—See notes to Table 3 for explanation of SB1–SB6.

REFERENCES

Antonucci, R. R. J. 1993, ARA&A, 31, 473
Bregman, J. N., Hogg, D. E., & Roberts, M. S. 1995, ApJ, 441, 561
Broadhurst, T. J. 1989, Ph.D. thesis, Univ. Durham
Broadhurst, T. J., Ellis, R. S., & Glazebrook, K. 1992, Nature, 335, 55
Broadhurst, T. J., Ellis, R. S., & Shanks, T. 1988, MNRAS, 235, 827
Bruzual A, G., & Charlot, S. 1993, ApJ, 405, 538
Burstein, D., Bertola, F., Buson, L. M., Faber, S. M., & Lauer, T. R. 1988, ApJ, 328, 440
Burstein, D., & Heiles, C. 1984, ApJS, 54, 33
Calzetti, D., Bohlin, R. C., Kinney, A. L., Storchi-Bergmann, T., & Heckman, T. M. 1995, ApJ, 443, 136
Calzetti, D., Kinney, A. L., & Storchi-Bergmann, T. 1994, ApJ, 429, 582
Charlot, S., Worthey, G., & Bressan, A. 1996, ApJ, 457, 625
Coleman, G. D., Wu, C.-C., & Weedman, D. W. 1980, ApJS, 43, 393
Condon, J. J., Condon, M. A., Gisler, G., & Puschell, J. J. 1982, ApJ, 252, 102
Connolly, A. J., Szalay, A. S., Bershady, M. A., Kinney, A. L., & Calzetti, D. 1995, AJ, 110, 1071
Fabbiano, G. 1989, ARA&A, 27, 87
Fabbiano, G., Kim, D.-W., & Trinchieri, G. 1992, ApJS, 80, 531
Giavalisco, M., Macchetto, F. D., & Sparks, W. B. 1994, A&A, 288, 103
Gunn, J. E., & Knapp, G. R. 1992, PASP, 43, 267
Israel, F. P., & van der Hulst, J. M. 1983, AJ, 88, 1736
Kennicutt, R. C. 1992, ApJS, 79, 255
King, C. R., & Ellis, R. S. 1985, ApJ, 288, 456
Kinney, A. L., Bohlin, R. C., Calzetti, D., Panagia, N., & Wyse, R. F. G. 1993, ApJS, 86, 5

Koo, D. C., & Kron, R. G. 1992, ARA&A, 30, 613
Koratkar, A. P., Bohlin, R. C., Calzetti, D., & Kinney, A. L. 1996, in preparation
Lawrence, A., & Elvis, M. 1982, ApJ, 256, 410
Leitherer, C., & Heckman, T. M. 1995, ApJS, 96, 38
McQuade, K., Calzetti, D., & Kinney, A. L. 1995, ApJS, 97, 331
Pedlar, A., Booler, R. V., Specer, R. E., & Stewart, O. J. 1983, MNRAS, 202, 647
Pence, W. 1976, ApJ, 203, 39
Pier, E., & Krolik, J. 1992, ApJ, 401, 99
Roche, P. F., Aitken, D. K., Smith, C. H., & Ward, M. J. 1991, MNRAS, 248, 606
Sadler, E. M. 1984, AJ, 89, 53
Sanders, D. B., Phinney, E. S., Neugebauer, G., Soifer, B. T., & Mathews, K. 1989, ApJ, 347, 29
Schechter, P. 1976, ApJ, 203, 297
Seaton, M. J. 1979, MNRAS, 187, 73P
Steidel, C. C., & Hamilton, D. 1992, AJ, 104, 941
———. 1993, 105, 2017
Storchi-Bergmann, T., Kinney, A. L., & Challis, P. 1995, ApJS, 98, 103
Subrahmanya, C. R., & Harnett, J. I. 1987, MNRAS, 225, 297
Ulvestad, J. S., & Wilson, A. S. 1984, ApJ, 285, 439
Weedman, D. W., Feldman, F. R., Balzano, V. A., Ramsey, L. W., Sramek, R. A., & Wu, C.-C. 1981, ApJ, 248, 105
Wirtz, V. C. 1918, Astron. Nachr., 206, 109